THE STELLAR KINEMATICS IN THE SOLAR NEIGHBORHOOD FROM LAMOST DATA

Hai-Jun Tian[1,2], Chao Liu[2], Jeffrey L. Carlin[3,4], Yong-Heng Zhao[2], Xue-Lei Chen[2], Yue Wu[2], Guang-Wei Li[2], Yong-Hui Hou[5], and Yong Zhang[5]

[1] China Three Gorges University, Yichang, 443002, China
[2] Key Laboratory of Optical Astronomy, National Astronomical Observatories, Chinese Academy of Sciences, Beijing 100012, China
[3] Department of Physics, Applied Physics and Astronomy, Rensselaer Polytechnic Institute, 110 8th Street, Troy, NY 12180, USA
[4] Department of Physics and Astronomy, Earlham College, 801 National Road West, Richmond, IN 47374, USA
[5] Nanjing Institute of Astronomical Optics & Technology, National Astronomical Observatories, Chinese Academy of Sciences, Nanjing 210042, China

ABSTRACT

We use about 200,000 FGK-type main-sequence stars from the LAMOST DR1 data to map the local stellar kinematics. With the velocity deprojection technique, we are able to derive the averaged three-dimensional velocity and velocity ellipsoids using only the line-of-sight velocity for the stars with various effective temperatures within $100 < |z| < 500$ pc. Using the mean velocities of the cool stars, we derive the solar motion of $(U_\odot, V_\odot, W_\odot) = (9.58 \pm 2.39, 10.52 \pm 1.96, 7.01 \pm 1.67)$ km s^{-1} with respect to the local standard of rest. Moreover, we find that the stars with $T_{\rm eff} > 6000$ K show a net asymmetric motion of ~ 3 km s^{-1} in $\langle W \rangle$ compared to the stars with $T_{\rm eff} < 6000$ K. And their azimuthal velocity increases when $|z|$ increases. This peculiar motion in the warmer stars is likely because they are young and not completely relaxed, although other reasons, such as the resonance induced by the central rotating bar or the spiral structures and the perturbation of the merging dwarf galaxies, cannot be ruled out. The derived velocity dispersions and cross-terms for the data are approximately consistent with previous studies. We also find that the vertical gradients of σ_U and σ_V are larger than that of σ_W. And the vertical gradient of σ_U shows a clear correlation with $T_{\rm eff}$, while the other two do not. Finally, our sample shows a vertex deviation of about $11°$ at $300 < |z| < 500$ pc, but roughly zero at $100 < |z| < 300$ pc.

Key words: Galaxy: disk – Galaxy: evolution – Galaxy: fundamental parameters – Galaxy: kinematics and dynamics – solar neighborhood

1. INTRODUCTION

The velocity distribution of the stars in the solar neighborhood plays a key role in understanding the global structure, dynamical features, and evolution of the Milky Way. Although it is often approximated with a multidimensional Gaussian profile, the velocity distribution of the stars in the solar neighborhood is actually very complicated. The mean value of the velocity distribution should be around zero, given that the Galactic disk is in a static state. However, observations have found many substructures (Dehnen 1998; Zhao et al. 2009; Siebert et al. 2011; Antoja et al. 2012; Xia et al. 2014), which may be associated with the perturbation of the Galactic bar and spiral arms or belong to old tidal debris of disrupted clusters or dwarf galaxies (Dehnen 2000; Fux 2001; Famaey et al. 2005; Antoja et al. 2011), in the velocity distribution. These substructures may shift the mean velocity slightly away from zero by a few km s^{-1}.

Recently, Widrow et al. (2012) found that the stellar number density is not symmetric with respect to the Galactic midplane, implying a vertical wave in the stellar disk. Gómez et al. (2013) inferred that the merging event of the Sagittarius dwarf galaxy can induce such density waves. The vertical asymmetry in stellar count may be associated with vertical asymmetry in velocity. Indeed, Carlin et al. (2013) found from the LAMOST DR1 data that not only radial velocity but also the vertical velocity of the nearby stars is not symmetric. These new observational evidences challenge the current dynamical models of the disk. At least some of the nearby disk stars are not in equilibrium, although the majority must be in the static state so that the Galactic disk can survive over billions of years. More investigation is required to figure out how many and

which types of stars contribute to the asymmetric motion, which is our main motivation of this work.

The velocity distribution can be characterized by the velocity ellipsoid, which reflects the mass distribution and evolution of the Milky Way, assuming that most of the detected stars are in equilibrium. The earliest study of the stellar velocity ellipsoid was done by Schwarzschild (1908). From then on, many works have found that the age of stars is correlated with the velocity distribution. Specifically, older stars show larger velocity dispersion, and vice versa (Parenago 1950; Roman 1950, 1952; Dehnen & Binney 1998; Quillen & Garnett 2001; Nordström et al. 2004; Holmberg et al. 2007, etc.). This is usually thought to be because scattering of the disk stars increases over time. For the stars younger than ~ 8 Gyr, the scattering is most likely due to encounters with substructures, e.g., giant molecular clouds, in the disk (Holmberg et al. 2007). The age–velocity dispersion relation (AVR) reflects the evolution history of the Galactic disk.

In an ideal axisymmetric disk, the velocity ellipsoid near the disk midplane should be aligned with the cylindrical coordinates. However, since the Galactic disk contains a rotational central bar and a number of spiral arms, the velocity ellipsoid will not match this ideal case. On the contrary, it deviates from the cylindrical coordinates near the Galactic midplane. Dehnen & Binney (1998, hereafter DB98) reported that the vertex deviation of the velocity ellipsoid measured from *Hipparcos* proper-motion data is $\sim 10°$. Smith et al. (2012, hereafter S12) confirmed that the vertex deviation of the metal-rich stars in the SDSS sample is consistent with DB98. Moreover, the authors also showed that the tilt angle relative to the Galactic midplane is about -10 to $-15°$ for the velocity ellipsoid at $z > 0.5$ kpc. Recently, lots of new works have been

done with the data from large stellar spectroscopic surveys, e.g., Binney et al. (2014) and Sharma et al. (2014) based on RAVE (Kordopatis et al. 2013), Bovy et al. (2014) based on APOGEE (Ahn et al. 2014), and Recio-Blanco et al. (2014) based on the *Gaia*-ESO survey (Gilmore et al. 2012).

Since 2011, the LAMOST survey (Cui et al. 2012; Deng et al. 2012; Zhao et al. 2012) has been operating, and about 1 million stellar spectra with stellar parameters have been released in the DR1 catalog. A large fraction of these stars are located within 1 kpc around the Sun, providing a vast resource to reveal details of the local stellar velocity distribution and give constraints on the dynamical structure and evolution of the Galactic disk.

In this paper, we use the FGK-type main-sequence stars selected from the LAMOST DR1 catalog to study the local velocity distribution. We use the effective temperature of these stars as a proxy for age and investigate the variation of the velocity distribution, including the mean velocity and the velocity ellipsoid, as a function of the effective temperature and height above/below the Galactic mid-plane.

The paper is organized as follows. In Section 2, we describe how we select the samples. In Section 3, we introduce a velocity deprojection method to reconstruct the velocity and velocity ellipsoid in three dimensions from only the line-of-sight velocity. The method is then validated with GCS data and a mock catalog. The systematic biases due to the uneven spatial sampling and the spatial variation of the velocity ellipsoid are then calibrated. The mean velocities and velocity ellipsoids in various effective temperature bins at different heights are then derived and discussed in Sections 4 and 5. Finally, brief conclusions are drawn in Section 6.

2. THE DATA

2.1. The LAMOST Survey

LAMOST is a quasi-meridian reflecting Schmidt telescope with an effective aperture of about 4 m and a field of view of 5°, operated by the National Astronomical Observatories, Chinese Academy of Sciences. It is a powerful instrument to survey the sky with the capability of recording 4000 spectra simultaneously (Cui et al. 2012; Zhao et al. 2012). In its five-year survey plan, it will obtain a few million stellar spectra in about 20,000 square degrees in the northern hemisphere (Deng et al. 2012).

The LAMOST Survey has internally delivered the first data release (DR1), which contains 2,204,860 spectra with a resolution of ∼1800 covering a wavelength range of $3800 \lesssim \lambda \lesssim 9100$ Å. The catalog contains 1,085,404 stellar spectra with estimated stellar atmospheric parameters and line-of-sight velocities. The distances to stars with estimated effective temperature, surface gravity, and metallicity are determined from isochrone fitting by Carlin et al. (2015). They developed two techniques, chi-square and Bayesian, to estimate the absolute magnitude. The chi-square technique finds the best-fit absolute magnitude that reaches the minimum of the chi-square between the measured T_{eff} log g, [Fe/H] and the isochrone ones. The Bayesian technique, on the other hand, considers both the selection effect and the different stellar populations along different lines of sight. They verified that the accuracies of the distance estimates derived from both techniques are ∼20%. They also found that their method may underestimate the distance of the giant stars by about 20%,
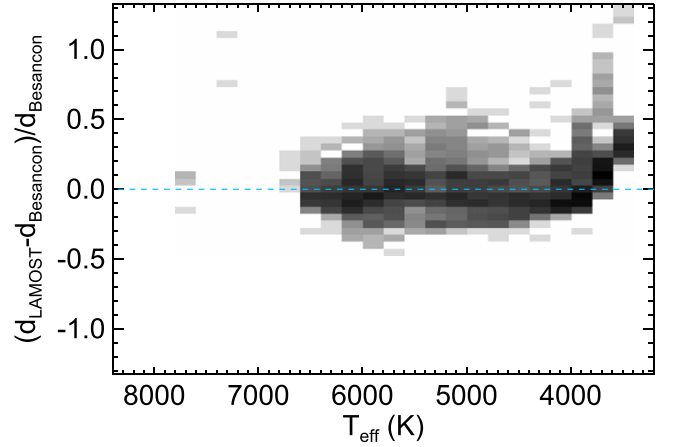

Figure 1. Fractional distance residuals resulting from running the Carlin et al. (2015) distance code on a realizations of the Besancon model in a field at $(l, b) = (180°, 60°)$.
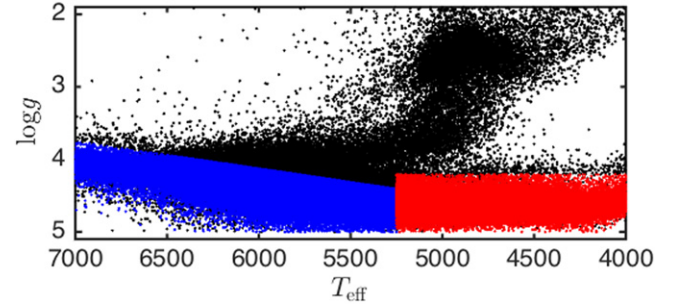

Figure 2. Distribution of the LAMOST DR1 stars in the T_{eff} vs. log g plane. The black points are all stars in the LAMOST DR1 with a signal-to-noise ratio of S/N > 10 in g band. The blue and red points are the main-sequence stars selected for this work.

but for main-sequence stars with $4000 < T_{eff} < 7000$ K no correlation is found with T_{eff}, as presented in Figure 1. Compared with the *Hipparcos* data, they obtained fairly good distance estimates with scatter of only ∼17%. Considering that only the FGK main-sequence stars are used in this work, the accuracy of the distance is sufficient for the studies of the local stellar kinematics within about 1 kpc. For such nearby stars, no significant difference is found between the two techniques. Therefore, we adopt the distance estimates from the chi-square technique in this work.

2.2. The Sample Selection

We select nearby FGK-type main-sequence stars to investigate the kinematics of the solar neighborhood. In order to select main-sequence stars, we define the selection criteria separately for stars with T_{eff} larger and smaller than 5250 K. For the stars with T_{eff} higher than 5250 K (displayed by the blue dots in Figure 2), the selection criteria are as follows:

1. $5250 < T_{eff} < 7000$ K,
2. log $g > (3.75–4.5)/(7000–5000)^*(T_{eff}–5000) + 4.5$,
3. $(−T_{eff}/500 + 14.1) < M_J < (−T_{eff}/550 + 15.0)$,

where M_J is the estimated absolute magnitude in J band from Carlin et al. For stars with $T_{eff} < 5250$ K (presented by the red points in Figure 2), the criteria are as follows:
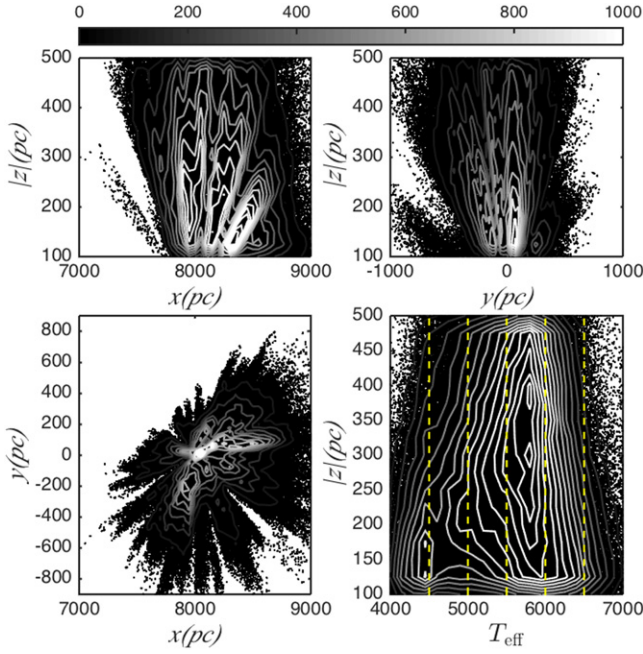
1. $4000 < T_{eff} < 5250$ K,

Figure 3. Distribution of the sample in galactocentric Cartesian coordinates. The top left (x–$|z|$), top right (y–$|z|$), and bottom left (x–y) panels shows the projected distributions, respectively. The Sun is located at $(x, y, z) = (8.0, 0, 0)$ kpc. The bottom right panel shows the stellar distribution in the $T_{\rm eff}$ vs. $|z|$ plane. The five vertical dashed lines divide $T_{\rm eff}$ into six bins, in which the velocities and their dispersions are determined in this work. The contours represent the number of stars with different levels.

2. $\log g > 4.2$,
3. $(-T_{\rm eff}/700 + 11.0) < M_J < (-T_{\rm eff}/750 + 12.0)$.

The criteria on $\log g$ and M_J are empirically set to ensure that the selected stars are in the main sequence. The criteria for higher $T_{\rm eff}$ remove the possible subgiant branch stars so that the rest of the warm main-sequence stars may better trace the young populations. The criteria for lower $T_{\rm eff}$ exclude the giant stars. We further select stars whose spectra have signal-to-noise ratio higher than 10 in the g band, which is the most sensitive portion of the spectrum to the stellar parameters. We also select the stars within

1. $100 < |z| < 500$ pc,
2. $7 < R_{GC} < 9$ kpc,

adopting the position of the Sun to be $(X, Y, Z) = (8, 0, 0)$ kpc. The stars within 100 pc are not well observed in the LAMOST survey because most of these stars are too bright. Therefore, we only select the stars with $|z| > 100$ pc. Finally, a total of 209,316 FGK-type main-sequence stars are selected after applying all above criteria. It is worthwhile to point out that this sample is significantly extended compared to the previous works (DB98; S12; Nordström et al. 2004; Siebert et al. 2008; Büdenbender et al. 2014, etc.). Therefore, the statistics based on such a large sample may be substantially improved, and the sample containing a wide range of effective temperatures allows us to map the detailed kinematics for variant spectral types. Figure 3 shows the distribution of the sample in the Cartesian coordinate system with respect to the Galactic center (the top left, top right, and bottom left panels) and the $T_{\rm eff}$ versus $|z|$ plane (the bottom right panel). The five vertical dashed lines in the bottom right panel divide the effective temperature into six bins, in which the stellar kinematics are
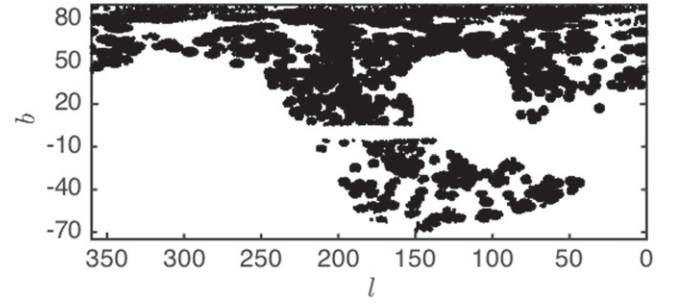

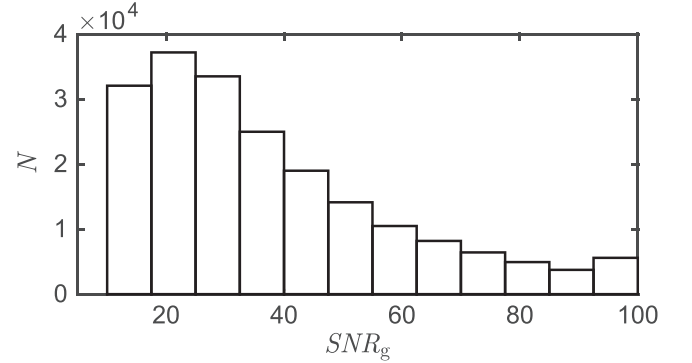**Figure 4.** Distribution of the sample in the l vs. b plane.

Figure 5. Distribution of the signal-to-noise ratio in g band of the sample.

determined separately in the later sections. Figure 4 presents the distribution of the sample in the l versus b plane. From these figures, it is clear that the stars are not uniformly distributed in the sky. This leads to a distortion of the measured velocity ellipsoid, which is discussed in Section 3.3.2. Figure 5 displays that most of the selected stars have a signal-to-noise ratio in g band larger than 10.

2.3. The Radial Velocity

The LAMOST catalog provides the radial velocity of each star with uncertainty of about 5 km s^{-1} (Gao et al. 2014). In order to investigate the systematics of the radial velocities, we cross-identify the LAMOST data with the APOGEE data released in SDSS DR10 (Ahn et al. 2014) and find ~1000 common stars with good parameter estimates and velocity scatter smaller than 0.3 km s^{-1} (which removes most multiple or variable stars) from APOGEE and signal-to-noise ratio higher than 20 in the LAMOST spectra. The radial velocity derived from the LAMOST pipeline is slower by 5.7 km s^{-1} compared with APOGEE, as shown in Figure 6. The reason for this offset is unclear and is worthy of further investigation in future works. In this work, we simply add an additional 5.7 km s^{-1} to the LAMOST-derived radial velocity to match the other survey data. It is noted that the offset is weakly anticorrelated with $T_{\rm eff}$, but there is no significant correlation with [Fe/H] and $\log g$. We further investigate whether the weak anticorrelation with $T_{\rm eff}$ changes our result in Section 5.4.

3. THE METHOD

For most of the LAMOST data, the proper motions can be found from either the UCAC4 (Zacharias et al. 2013) or PPMXL (Röser et al. 2010) catalog. However, because the purpose of this work is to derive the velocity ellipsoids, it
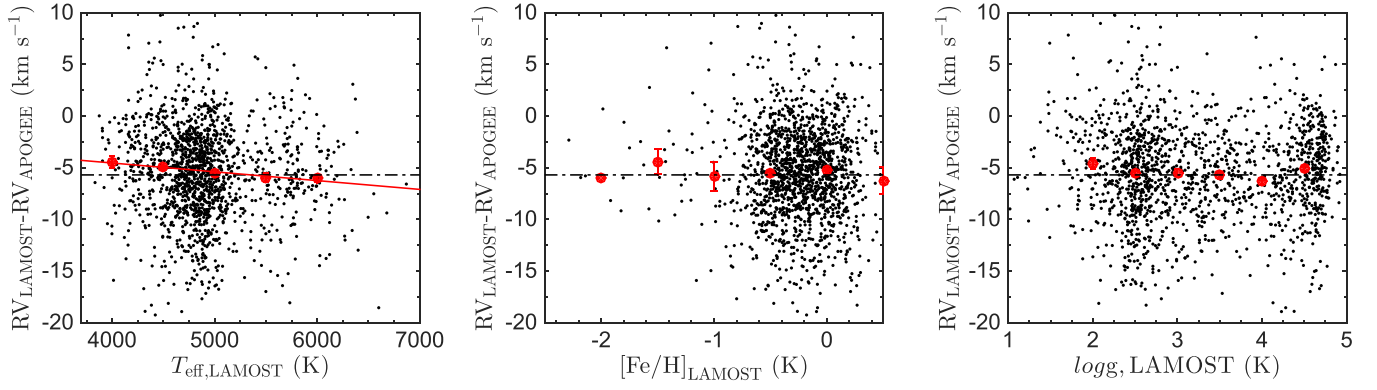
Figure 6. Left: offset of the radial velocity between LAMOST and APOGEE as a function of the LAMOST $T_{\rm eff}$. The black dots are the individual stars, and the red filled circles are the median values in each $T_{\rm eff}$ bin. The red line indicates the best linear fit of the median points. The black dot-dashed line marks the location of the average offset of 5.7 km s^{-1}. Middle: offset of the radial velocity as a function of the LAMOST [Fe/H]. The symbols are similar to those in the left panel. No clear correlation is found in this plot. Right: offset of the radial velocity as a function of the LAMOST $\log g$. The symbols are similar to those in the left panel.

requires accurate measurement of the uncertainties of the proper motions, as well as the values themselves. Unfortunately, after tentatively measuring the three-dimensional velocities and their ellipsoids with the combination of the proper motions and the radial velocity, we find that the errors of these proper motions are too large to derive the reliable velocity ellipsoids. Therefore, we turn to measuring the three-dimensional velocity and its ellipsoid from only the one-dimensional line-of-sight velocities of the LAMOST sample spanning a large area of the sky. In this section, we first describe the velocity deprojection method and then discuss the validation and calibration of the approach.

3.1. The Deprojection Method

Consider a star with the line-of-sight unit vector $\boldsymbol{r}$ and heliocentric velocity of $\boldsymbol{v}$. The observed line-of-sight velocity $v_{\rm los}$ can be written as

$$v_{\rm los} = \boldsymbol{r} \cdot \boldsymbol{v}. \tag{1}$$

$\boldsymbol{r}$ is determined by the Galactic coordinates l and b, and the three components of $\boldsymbol{v}$ in the galactocentric Cartesian coordinates are U, V, and W, respectively. Then Equation (1) can be expanded as

$$v_{\rm los} = U \cos l \cos b + V \sin l \cos b + W \sin b. \tag{2}$$

Given a group of stars at similar distances along the line of sight $\boldsymbol{r}$, the velocity dispersion projected onto the line of sight should be

$$\sigma_{\rm los}^2 = \frac{\sum_{i=1}^{N}\big(\boldsymbol{r}_i \cdot (\boldsymbol{v}_i - \bar{\boldsymbol{v}})\big)^2}{N}, \tag{3}$$

where N is the number of the stars. This can be specified as

$$
\begin{aligned}
\sigma_{\rm los}^2 = {} & \sigma_U^2 \cos^2 l \cos^2 b + \sigma_V^2 \sin^2 l \cos^2 b + \sigma_W^2 \sin^2 b \\
& + \sigma_{UV}^2 \sin 2l \cos^2 b + \sigma_{UW}^2 \cos l \sin 2b \\
& + \sigma_{VW}^2 \sin l \sin 2b,
\end{aligned} \tag{4}
$$

where the dispersions σ_U, σ_V, and σ_W specify the size and shape of the velocity ellipsoids, and the cross-terms σ_{UV}, σ_{UW}, and σ_{VW} determine the orientation of the velocity ellipsoids.

3.2. The Likelihood

According to Equations (2) and (4), one is able to reconstruct the 3D mean velocity and velocity ellipsoid at a given spatial position from the line-of-sight velocities of a group of stars located at the same position. To do this, we construct a likelihood as follows:

$$L = \prod_{k=1}^{N} \left\{ \frac{1}{\sqrt{\sigma_{{\rm model},k}^2 + \epsilon_k^2}} \exp\left[-\frac{(v_{{\rm los},k} - v_{{\rm model},k})^2}{2\big(\sigma_{{\rm model},k}^2 + \epsilon_k^2\big)} \right] \right\}, \tag{5}$$

where $v_{{\rm los},k}$ is the measured line-of-sight velocity of the kth star, $\epsilon_{{\rm los},k}$ is the measured error of the line-of-sight velocity, and $v_{{\rm model},k}$ and $\sigma_{{\rm model},k}$ are the predicted mean line-of-sight velocity and the projected velocity dispersion along the line of sight of the kth star, respectively. The following nine quantities, U, V, W, σ_U, σ_V, σ_W, σ_{UV}, σ_{UW}, and σ_{VW}, are free parameters in Equation (5). The best-fit values for them can be found by maximizing the likelihood L.

We use the Markov chain Monte Carlo (MCMC) simulation to estimate the posterior probabilities of the velocities and the velocity ellipsoids. The priors of the three mean velocities, U, V, and W, are evenly distributed in all real values, while the priors of the velocity ellipsoids are evenly distributed in the range of $(0, +\infty)$. In this work, we run the MCMC simulation with *emcee*, which implements the affine-invariant ensemble sampler (Goodman & Weare 2010; Foreman-Mackey et al. 2012).

3.3. Validation of the Method

The velocity deprojection technique has been applied by DB98, who used the proper motions of *Hipparcos* to estimate the velocity and dispersions of stars with median distance of ~70 pc around the Sun. Later, Fuchs et al. (2009) applied a similar method to the SDSS data, which extends to a few hundred parsecs away from the Sun. However, McMillan & Binney (2009) then pointed out that the deprojection technique may produce systematic bias in the cross-terms, especially in σ_{UW}, if σ is a function of R and z. Because our method is very similar to that DB98 used and our data are located between 100 and 500 pc in $|z|$, we may also suffer from

similar biases. Furthermore, unlike the *Hipparcos* data, the highly uneven spatial distribution of the LAMOST data may lead to another systematic bias. Therefore, before applying this method to the LAMOST data, we need to carefully validate it and understand these issues.

3.3.1. Validation with GCS Data

Our first validation uses data from the Geneva-Copenhagen Survey (GCS; Nordström et al. 2004), which is a volume-complete set of F- and G-type stars within ∼40 pc, and provides three-dimensional velocity components for each individual star. This data set does not extend to a large volume; hence, it may not be severely affected by the systematic bias explained by McMillan & Binney (2009). Thus, we expect that the deprojection method may give estimates close to the true values.

A subsample of 3712 dwarf stars for the validation test is selected from GCS data with $5500 \, \mathrm{K} < T_{\mathrm{eff}} < 6000 \, \mathrm{K}$, $|U| < 200 \, \mathrm{km \, s^{-1}}$, $|V| < 400 \, \mathrm{km \, s^{-1}}$, and $|W| < 200 \, \mathrm{km \, s^{-1}}$. Outliers beyond 4σ in the line-of-sight velocity distribution are removed. Only the line-of-sight velocity of these data is used to derive their mean velocities and velocity ellipsoid according to Equation (5) via MCMC simulation. In order to reduce the effect of the uneven distribution on the sky, we separate the sky into small equal-area bins and randomly select roughly equal numbers of stars in each bin so that the samples are approximately evenly distributed on the whole sky. We repeat the arbitrary draw of the data in equal-area bins 40 times and estimate the velocity and its ellipsoid for each random drawing with MCMC. The final derived velocities and velocity dispersions are the averaged values over the 40 random draws. Uncertainties on the velocities and their dispersions are composed of two parts: (1) the internal error from the MCMC, and (2) the external error due to the selection of the sample. The total uncertainties of the derived values are the square root of the quadratic sum of the two parts. We compare the best-fit values with the true values directly measured from the U, V, and W of the individual stars (see Table 1) and find that the derived velocities and the ellipsoid are in good agreement with the true values. This confirms that the deprojection method can reconstruct the 3D kinematics for the stars within a very local volume.

3.3.2. Validation with the Mock Data

LAMOST data are neither volume complete nor completely cover the whole 4π sky area. This subsequently leads to large spatial distortion in the velocity deprojection method since many lines of sight are not observed. Moreover, the LAMOST data in this work spread from 100 to 500 pc in $|z|$, far beyond the volume of both GCS and *Hipparcos* data. The systematic bias due to the spatial variation of σ may be stronger in this larger volume, as pointed out by McMillan & Binney (2009). In order to investigate both sources of systematics, we introduce a second test, assigning mock line-of-sight velocities from predefined velocity ellipsoids to data with the same spatial position as actual LAMOST stars. The random draws of the line-of-sight velocities are based on a presumed Gaussian distribution function in galactocentric cylindrical coordinates with mean velocity components of $[\langle v_R \rangle, \langle v_\phi \rangle, \langle v_z \rangle] = [0, -26,$

$0] \, \mathrm{km \, s^{-1}}$ and velocity dispersions of

$$\sigma(R, z) = \left(\sigma_{R_0} + 20z, \, \sigma_{\phi_0} + 20z, \, \sigma_{z_0} + 30z \right) \mathrm{km \, s^{-1}}$$
$$\times \exp\left[(R_0 - R)/R_\sigma \right], \tag{6}$$

where $R_0 = 8.0 \, \mathrm{kpc}$ is the galactocentric radius of the Sun, R_σ is set to $5 \, \mathrm{kpc}$, $\sigma_0 \equiv (\sigma_{R_0}, \sigma_{\phi_0}, \sigma_{z_0}) = (45, 32, 24) \, \mathrm{km \, s^{-1}}$ following McMillan & Binney (2009), and z is in kpc. The cross-terms $\sigma_{R\phi}$, σ_{Rz}, and $\sigma_{\phi z}^2$ are set to 0. For each observed star, its stellar parameters, as well as the three-dimensional positions, are kept the same as the observed values, but its three-dimensional velocity vector is randomly drawn from the Gaussian distribution function. The mock line-of-sight velocity for each star is then given by Equation (2), presuming that $U \cong -v_R$, $V \cong v_\phi$, and $W \cong v_z$ in the solar neighborhood.

The mock sample is first split out into three slices in height, i.e., $100 \, \mathrm{pc} < |z| < 300 \, \mathrm{pc}$, $200 \, \mathrm{pc} < |z| < 400 \, \mathrm{pc}$, and $300 \, \mathrm{pc} < |z| < 500 \, \mathrm{pc}$. The overlap between neighboring slices can help to smooth the results. Then each $|z|$ slice is again split out into six bins in effective temperature with an interval of $500 \, \mathrm{K}$ ranging from 4000 to 7000 K. Here we assume that the mean velocity components and velocity ellipsoids are the same for stars within the same T_{eff} bin in each $|z|$ slice. The results are displayed in Figure 7, with the solid lines representing the derived values and dashed lines for the true values. Because the velocity dispersions are functions of $|z|$ and stars with different effective temperatures have different spatial distributions, the true values are not strictly flat but show a slight bend with T_{eff}. The reconstructed $\langle U \rangle$, $\langle V \rangle$, and $\langle W \rangle$ are consistent with the true values. However, neither the velocity dispersions nor the cross-terms are in agreement with the true values. Although McMillan & Binney (2009) showed similar deviation in the cross-terms, their test did not demonstrate the bias in the velocity dispersions. The inhomogeneous distribution in sky position of the LAMOST data sample (see Figure 3), which can induce even stronger geometric distortion, may be responsible for the deviation in the velocity dispersions.

3.4. Calibration of the Derived Velocity Ellipsoid

In general, the distortion in the velocity ellipsoid due to the unevenly distributed sample can be modeled as skew and tilt on the true velocity ellipsoid. Therefore, the distortion can be corrected by a skew and tilt model, which can be mathematically presented as matrix transformations.

The outline of the calibration is as follows. First, the mock stars are selected to be exactly located in the same spatial positions of the observed stars, combined with the simulated velocities based on a known velocity distribution function, which is only qualitatively similar to the true one. Because the mock data are selected with the identical spatial distribution as the observed data, the true velocity ellipsoid of the mock data would be affected by the same skew and tilt as the observations. Thus, we can measure the extents of the skew and tilt from the quantitive differences between the deprojection-derived velocity ellipsoids and their true values for the mock data.

In the rest of this section, we denote that all quantities with subscripts $\cdot_o$, $\cdot_m$, $\cdot_t$, and $\cdot_c$ represent the observed values, the values measured from the mock data, the true values, and the corrected values, respectively. First, we correct the velocity

Table 1
Comparison of the Velocity Ellipsoids Derived from Different Methods for the GCS Data

	$\langle U \rangle$	$\langle V \rangle$	$\langle W \rangle$	$\langle \sigma_U \rangle$	$\langle \sigma_V \rangle$	$\langle \sigma_W \rangle$	$\langle \sigma_{UV} \rangle$	$\langle \sigma_{UW} \rangle$	$\langle \sigma_{VW} \rangle$
Direct	-9.86 ± 0.64	-23.49 ± 0.46	-7.57 ± 0.33	37.10 ± 0.58	25.69 ± 0.67	20.33 ± 0.37	11.04 ± 0.97	-6.37 ± 1.49	4.05 ± 2.39
Deprojection	-9.73 ± 3.01	-22.84 ± 0.74	-6.67 ± 1.22	35.40 ± 1.02	24.86 ± 0.95	18.97 ± 0.84	9.95 ± 2.04	-8.65 ± 5.79	3.17 ± 6.88

Note. The first line gives the results from the direct estimation, while the second row gives the results derived from the deprojection method.
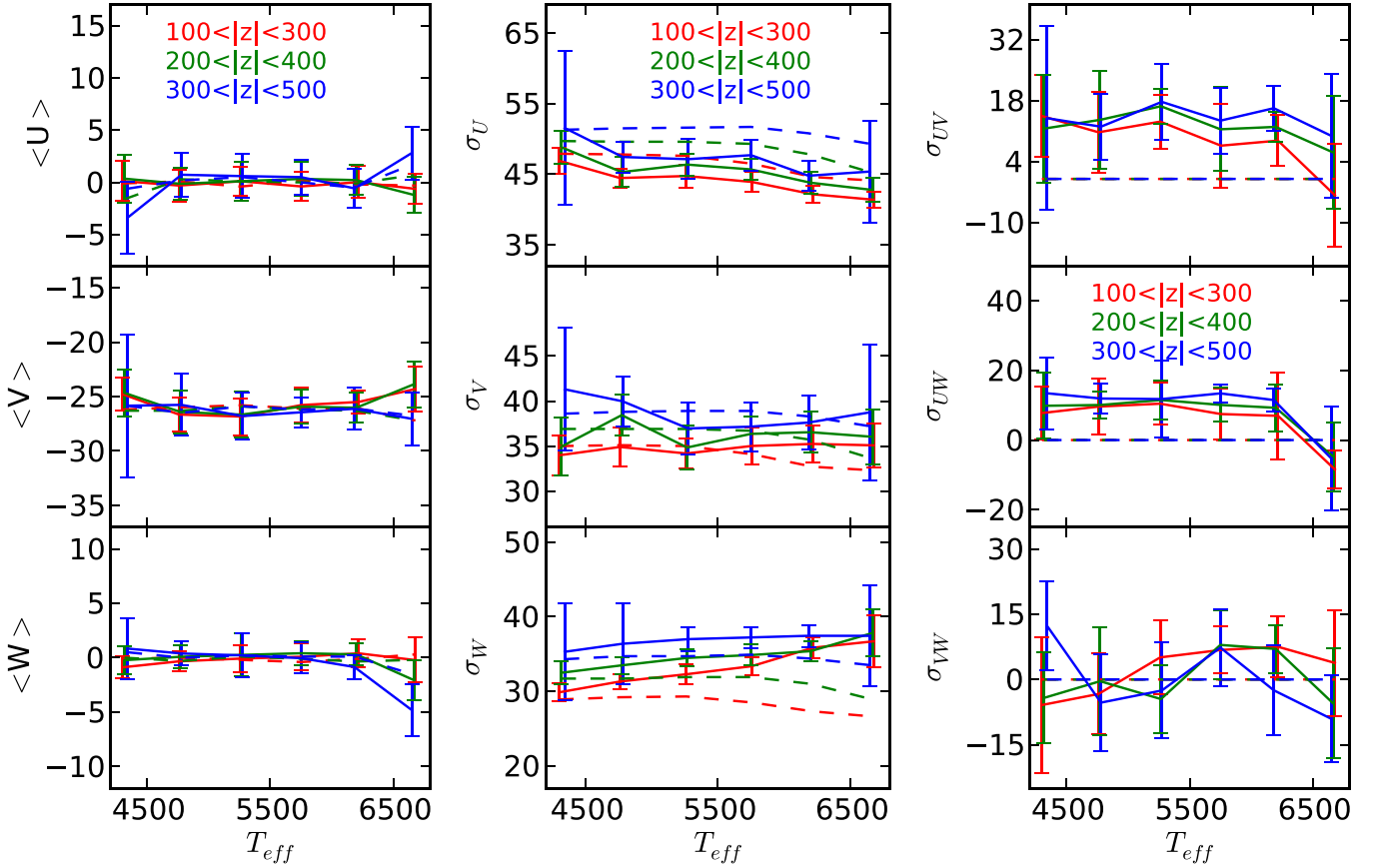
Figure 7. Comparison of the derived velocities and velocity dispersions with their true values for one of the six mock data sets. In all panels, the solid lines represent estimated values, while the dashed lines represent the true values of the mock data. Red, green, and blue indicate samples at $100 < |z| < 300$, $200 < |z| < 400$, and $300 < |z| < 500$ pc, respectively. The left panels present the three velocity components ($\langle U \rangle$, $\langle V \rangle$, and $\langle W \rangle$) in $T_{\rm eff}$ bins in each $|z|$ slice. The middle panels show the three velocity dispersions, and the right panels show the cross-terms.

vector with a simple offset:

$$v_c = v_o - \langle \Delta v \rangle, \qquad (7)$$

where $\langle \Delta v \rangle = \langle v_m - v_t \rangle$, which is derived by averaging over six simulations. Table 2 lists the mean offsets at different $T_{\rm eff}$ bins and $|z|$ slices. Most of the corrections are less than 1 km s^{-1}, implying that the distortion due to the unevenly distributed sample may not severely affect the derived mean velocities from the deprojection.

Next, we consider the velocity ellipsoids. For simplicity, we assume that the stars are in a three-dimensional Gaussian distribution. It is worth noting that this assumption is not physically true, because the asymmetric drift of the stars in the Galactic disk skews the azimuthal velocity to the slower side (Binney & Tremaine 2008). An approximation of a Gaussian distribution may derive a slower peak of the azimuthal velocity distribution. However, the derived V and σ_V based on the Gaussian approximation with the GCS data shown in Table 1 do not show obvious bias from the true values, implying that for the real observed data in the solar neighborhood, the Gaussian approximation may not contribute significant offsets in either V or σ_V. Therefore, we can still use a three-dimensional Gaussian profile to approximate the velocity distribution. A detailed investigation of the effect of the Gaussian approximation in the azimuthal velocity and its dispersion is discussed in Section 5.1.

We denote Σ_t and Σ_m as the true covariance matrices and the one derived with the mock data from the deprojection, respectively. Both can be rotated to align with the given axis by the following transform:

$$\boldsymbol{D}_t = \boldsymbol{V}_t^{-1} \Sigma_t \boldsymbol{V}_t$$
$$\boldsymbol{D}_m = \boldsymbol{V}_m^{-1} \Sigma_m \boldsymbol{V}_m, \qquad (8)$$

where $\boldsymbol{D}_t$ and $\boldsymbol{D}_m$ are diagonal matrices and $\boldsymbol{V}_t$ and $\boldsymbol{V}_m$ are the rotation transform matrices. The skew due to the inhomogeneity rescales the axis ratios and hence can be quantified by the division of the two diagonal matrices:

$$\boldsymbol{D}_t = \Lambda \boldsymbol{D}_m, \qquad (9)$$

where Λ is the scaled matrix. The tilt due to the inhomogeneity then can be quantified by the following transform:

$$\Sigma_t = \boldsymbol{V}_t \Lambda \boldsymbol{V}_m^{-1} \Sigma_m \boldsymbol{V}_m \boldsymbol{V}_t^{-1}. \qquad (10)$$

We define the correction matrices as $\boldsymbol{A} = \boldsymbol{V}_t \Lambda \boldsymbol{V}_m^{-1}$ and $\boldsymbol{B} = \boldsymbol{V}_m \boldsymbol{V}_t^{-1}$. Then, the observed velocity covariance Σ_o can be calibrated by

$$\Sigma_c = \boldsymbol{A} \Sigma_o \boldsymbol{B}. \qquad (11)$$

The calibration matrices can be derived from the simulations with mock data combining the observed 3D positions with arbitrarily drawn velocities from given velocity ellipsoids. In practice, the random mock data may introduce some statistical

Table 2
The Mean Offsets of Velocity to Calibrate the Geometric Distortion

T_{eff}	$\langle N \rangle$	$\langle \Delta U \rangle$	$\langle \Delta V \rangle$	$\langle \Delta W \rangle$
		$100 < |z| < 300$ pc		
4250	13229	0.66 ± 0.68	0.22 ± 0.89	-0.09 ± 0.41
4750	19593	-0.10 ± 0.25	-0.23 ± 0.29	-0.23 ± 0.34
5250	25805	0.38 ± 0.38	-0.27 ± 0.40	-0.01 ± 0.32
5750	33453	-0.29 ± 0.20	0.15 ± 0.42	0.06 ± 0.37
6250	23565	0.36 ± 0.31	0.48 ± 0.30	-0.18 ± 0.53
6750	6739	0.24 ± 0.79	1.96 ± 1.29	-0.90 ± 1.44
		$200 < |z| < 400$ pc		
4250	7600	2.44 ± 0.92	-0.22 ± 1.26	-0.31 ± 0.25
4750	16639	-0.26 ± 0.28	0.23 ± 0.73	0.05 ± 0.40
5250	27523	0.01 ± 0.32	0.10 ± 0.52	0.01 ± 0.23
5750	36303	-0.03 ± 0.27	0.27 ± 0.34	-0.05 ± 0.33
6250	18621	-0.22 ± 0.48	0.63 ± 0.63	-0.06 ± 0.46
6750	3436	-0.77 ± 0.92	2.13 ± 1.29	-0.15 ± 1.42
		$300 < |z| < 500$ pc		
4250	3797	0.58 ± 2.11	0.04 ± 1.17	-0.30 ± 0.48
4750	11443	-0.16 ± 0.43	0.47 ± 0.76	-0.38 ± 0.51
5250	22503	-0.41 ± 0.50	0.04 ± 0.59	-0.01 ± 0.26
5750	33595	0.06 ± 0.27	0.20 ± 0.40	-0.40 ± 0.30
6250	13986	-0.24 ± 0.91	0.58 ± 0.44	-0.73 ± 0.29
6750	1566	-1.81 ± 2.24	1.36 ± 1.83	0.44 ± 2.09

Note. The $\langle \Delta U \rangle$, $\langle \Delta V \rangle$, and $\langle \Delta W \rangle$ are the average offsets of the velocities for various T_{eff} bins at different $|z|$ slices.

fluctuations in **A** and **B**. Therefore, we run six simulations to generate six sets of **A** and **B**. The final calibrated velocity ellipsoid is averaged over the calibration by the six sets of transform matrices. Figure 8 shows the calibrated results, which are now consistent with their true values after the correction. It shows that not only the dispersions but also most of the cross-terms have been well reconstructed by the calibration. The calibration corrects the systematics raised from both the unevenly spatial distribution of the observed sample and the spatial variation of σ.

4. THE RESULTS OF THE LAMOST DR1 DATA

We apply the calibrated deprojection approach to the LAMOST data. Figure 9 and Table 8 show the results. The correlations of the three velocity and the six velocity ellipsoid components with T_{eff} are demonstrated in three slices of $|z|$, i.e., 100 pc $< |z| <$ 300 pc (red), 200 pc $< |z| <$ 400 pc (green), and 300 pc $< |z| <$ 500 pc (blue). The data at each $|z|$ slice are split out into 6 T_{eff} bins between $4000 < T_{\mathrm{eff}} < 7000$ K with an interval of 500 K. Similar to the procedure for GCS data described in Section 3.3.1, the uncertainty of the velocity and its ellipsoid is the square root of the quadratic sum of two parts: (1) the internal error from MCMC, and (2) the external error from the selection of the sample data on the sky. To measure the error from the second part, we run a 40-time bootstrap to randomly resample the observed data on the sky. For the mean velocities, the uncertainty is mainly from the first part, while for the second moments, the uncertainties are dominated by the second effect. In this sense, the final uncertainty of the velocity ellipsoid cannot be effectively reduced until the LAMOST

survey has covered a large, contiguous region of the northern sky, as it will by the end of the mission.

4.1. The Mean Velocities

The left panels of Figure 9 present the results of the three components of the average velocity ($\langle U \rangle$, $\langle V \rangle$, and $\langle W \rangle$).

The most obvious feature is that the three mean velocities shown in the left panels are all correlated with effective temperature for all $|z|$ bins. For the radial velocity $\langle U \rangle$ in the top left panel, at $T_{\mathrm{eff}} = 4250$ K, $\langle U \rangle$ is around 10–12 km s^{-1}, which is at around 0 km s^{-1} with respect to the local standard of rest (LSR; the black dashed line in the panel) adopting the solar motion of $U_\odot = 11.1$ km s^{-1} (Schönrich et al. 2010). In other T_{eff} bins, $\langle U \rangle$ for the stars within $100 < |z| < 300$ pc are approximately flat at around -9.07 to -8.74 km s^{-1}. For the stars in $200 < |z| < 400$ ($300 < |z| < 500$), on the other hand, $\langle U \rangle$ increases from -8.98 ± 1.47 (-9.37 ± 2.04) km s^{-1} at $T_{\mathrm{eff}} = 4750$ K to -6.49 ± 1.54 (-7.24 ± 2.09) km s^{-1} at $T_{\mathrm{eff}} = 6750$ K. Although the change of $\langle U \rangle$ from cool to warm is small, the increasing trend is quite clear, especially when $T_{\mathrm{eff}} > 6000$ K. The direction of $\langle U \rangle$ is toward the Galactic center; thus, the top left panel of Figure 9 indicates that either the warmer stars tend to move inward in the Galaxy or the cooler stars tend to move outward.

For the azimuthal velocity $\langle V \rangle$ in the middle left panel, the stars show a clear break at $T_{\mathrm{eff}} = 6000$ K. The stars cooler than 6000 K are located at around -30 km s^{-1}, while those warmer than 6000 K go abruptly up to around -20 km s^{-1}. This is another version of Parenago's discontinuity (Parenago 1950) and has been rediscovered by DB98 at $B - V = 0.61$, which corresponds to $T_{\mathrm{eff}} \sim 6000$ K according to Sekiguchi & Fukugita (2000). The cooler stars are, on average, older than the warmer stars, and hence most of them have had a longer time to experience scattering, which can increase the velocity dispersion and therefore increase the asymmetric drift (Jenkins 1992; Binney & Tremaine 2008). This leads to a slower azimuthal velocity for the older (cooler) stars. Another interesting feature is that the LAMOST data show an unusual gradient along $|z|$ for warmer stars. For the stars cooler than 6000 K, the azimuthal velocity decreases with $|z|$, while it turns out to increase with $|z|$ for the stars warmer than 6000 K. The former trend is natural since the stars at higher $|z|$ need more vertical energy and hence slightly lose their angular momenta and rotate more slowly, given that the stars are in equilibrium. However, it is difficult to understand why the warmer, or younger, stars show the trend turning around.

As did the other two velocity components, the vertical velocity $\langle W \rangle$ also shows a correlation with effective temperature. Compared to the zero velocity with respect to the LSR (shown as the black dashed horizontal line at 7.25 km s^{-1} Schönrich et al. 2010), the stars with $T_{\mathrm{eff}} < 5500$ K roughly stay around the zero point. However, the warmer stars with $T_{\mathrm{eff}} > 5500$ K show higher $\langle W \rangle$ than the zero point, i.e., they are moving toward the Galactic north pole up to $\langle W \rangle \sim -4$ km s^{-1}, which is equivalent to $+3$ km s^{-1} with respect to LSR. The stars located at larger $|z|$ seem to have a smaller $\langle W \rangle$ than those located in lower $|z|$, although the trend is not quite statistically significant.

The stars cooler than 6000 K over all $|z|$ bins are on average old. Since they do not show a significant gradient in $\langle V \rangle$, it is safe to assume that they are in equilibrium. Then, they can be used to determine the solar motion with respect to LSR. The
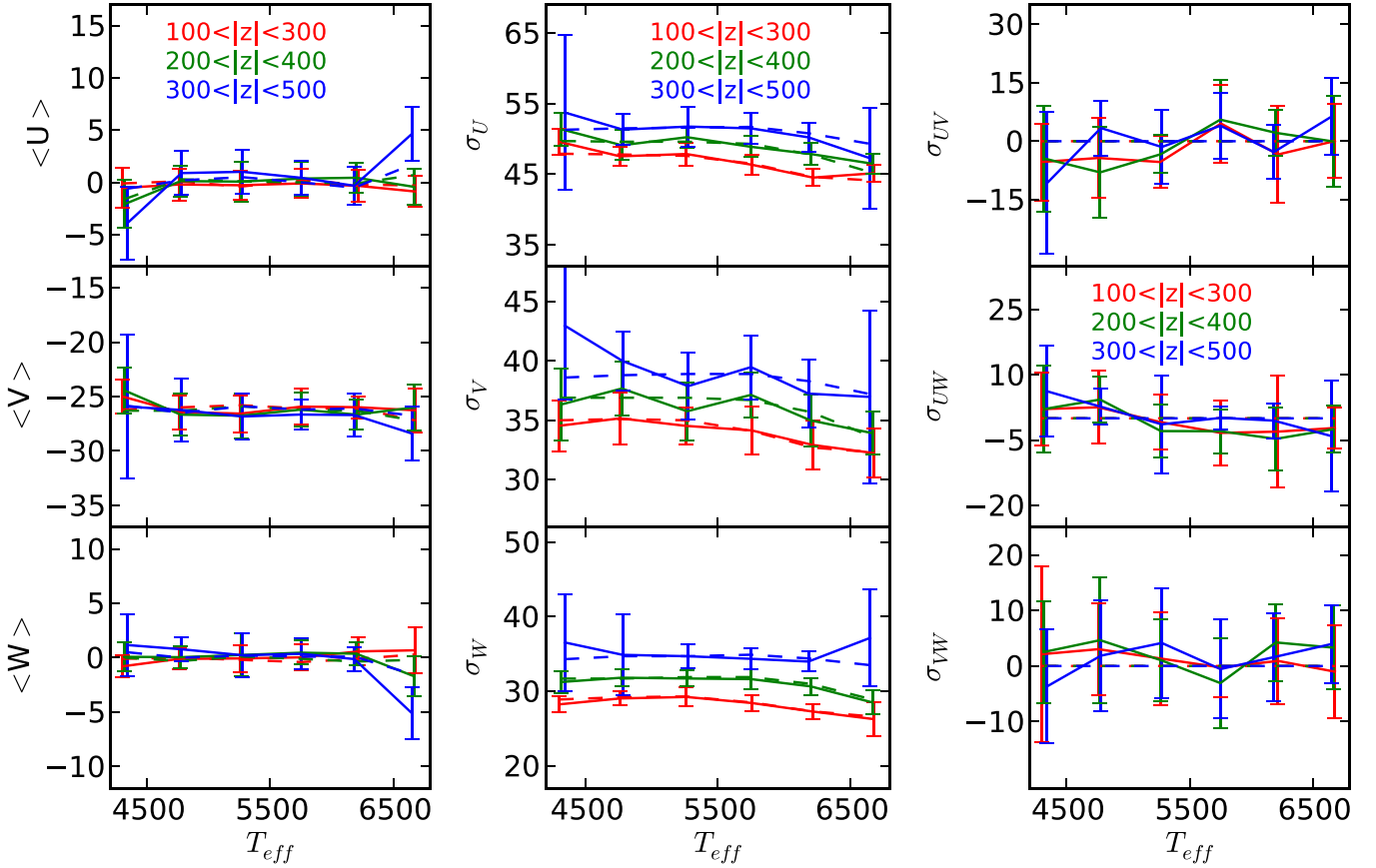
Figure 8. Same as Figure 7, but the estimated values have been calibrated via the method outlined in Section 3.4.

solar motion in radial and vertical directions can be derived from

$$U_{\mathrm{LSR}} = -\langle U \rangle$$
$$W_{\mathrm{LSR}} = -\langle W \rangle. \tag{12}$$

Thus, we directly obtain $U_\odot = 9.58 \pm 2.39$ km s^{-1} and $W_\odot = 7.01 \pm 1.67$ km s^{-1} by averaging over the $\langle U \rangle$ and $\langle W \rangle$ listed in the third and fifth columns of Table 8 for stars below 6000 K in all $|z|$ slices.

In order to estimate $V_\odot$, the asymmetric drift is required and a dynamical model has to be introduced. We start from Equation (4.228) of Binney & Tremaine (2008), which gives the approximation of the asymmetric drift from the circular speed, velocity dispersions, and the stellar density:

$$\overline{v}_s - V_\odot = v_a \simeq \frac{\overline{v_R^2}}{2v_c}$$

$$\left[\frac{\sigma_\phi^2}{\overline{v_R^2}} - 1 - \frac{\partial \ln\left(\nu \overline{v_R^2}\right)}{\partial \ln R} - \frac{R}{\overline{v_R^2}} \frac{\partial(\overline{v_R v_z})}{\partial z} \right], \tag{13}$$

where R is galactocentric radius, z is the height above the plane, v_c is the circular speed, and ν is the number density of stars, while a bar indicates the average value. Because the data are very close to the Galactic midplane, the cross-term of $\overline{v_R v_z}$ does not significantly vary with $|z|$ (Büdenbender et al. 2014), and therefore the last term of the equation is very small and can be negligible. Assume that the stellar density ν and σ_U are

exponential functions of R:

$$\nu \sim \exp\left(-\frac{R}{h_R}\right) \tag{14}$$

$$\sigma_U^2 \sim \exp\left(-\frac{R}{L}\right), \tag{15}$$

where h_R and L are scale length for the stellar density and σ_U, respectively. Then Equation (4.228) can be rewritten as

$$v_a \cong \frac{1}{2v_c}\left[\sigma_V^2 + \left(\frac{1}{h_R} + \frac{1}{L} - \frac{1}{R}\right)R\sigma_U^2\right]. \tag{16}$$

Therefore, the solar motion in V can be estimated from

$$V_\odot = -\left(\langle V \rangle + v_a\right). \tag{17}$$

Here we set $h_R = 2.6$ kpc following Jurić et al. (2008) or $h_R = 2.5$ kpc following Schönrich & Binney (2012) and Sharma et al. (2014). According to van der Kruit & Freeman (2011), L is equal to $2h_R$ given an isothermal disk. Although this relation has not been confirmed for the case of our Galaxy, it is a reasonable guess. As a comparison, the different case of $h_R = 3.0$ kpc and $L = 6.0$ kpc is also considered. The final results, including all three components, are listed in Table 3. Our estimates of the solar motion in three dimensions are in agreement with Schönrich et al. (2010) and Huang et al. (2015).

4.2. The Velocity Ellipsoids

The middle panels of Figure 9 show the velocity dispersions as functions of T_{eff} and $|z|$, and the right panels show the
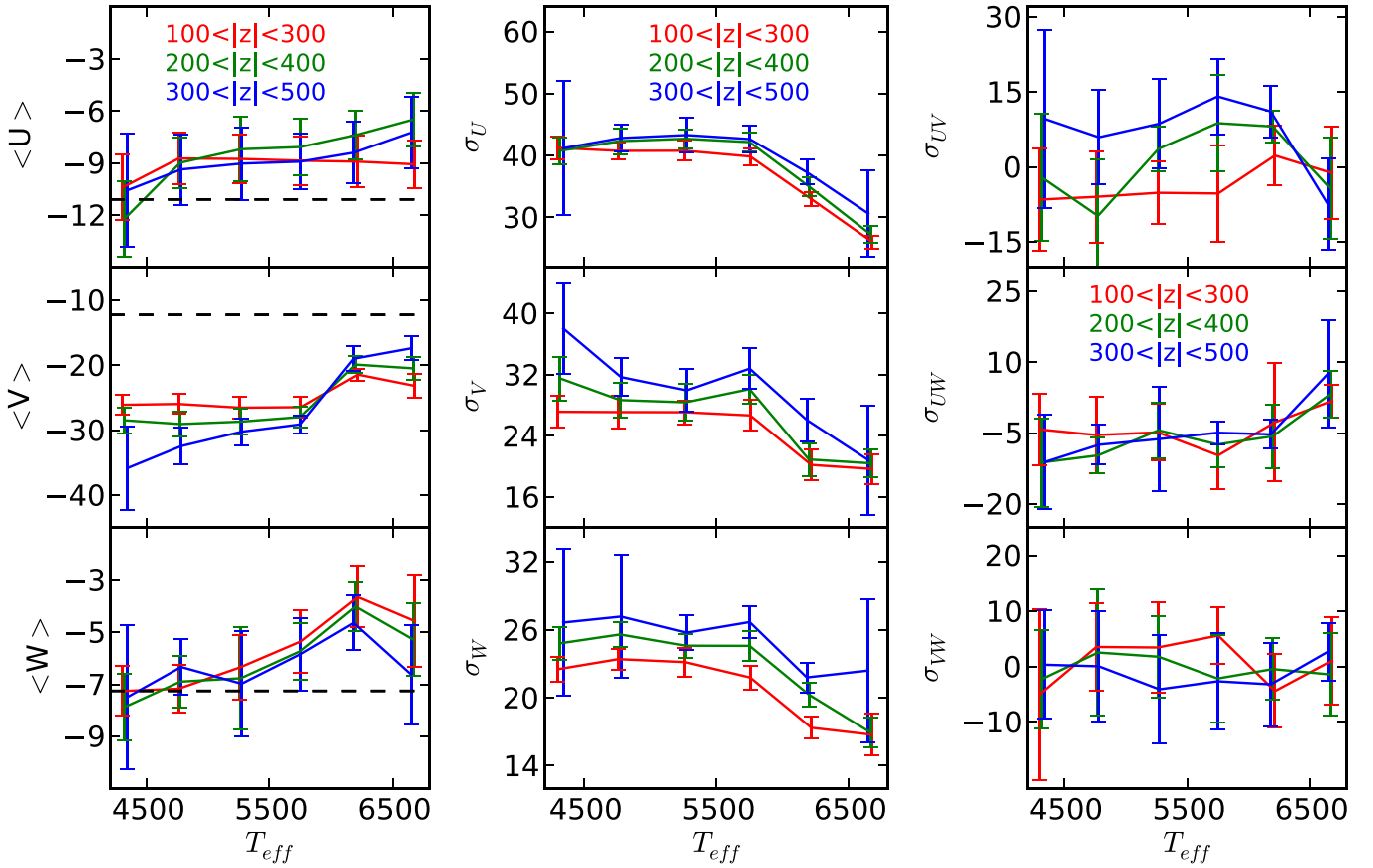
Figure 9. Mean velocities and velocity ellipsoids estimated from the LAMOST DR1 samples. The symbols are the same as in Figure 7. The three black dashed lines in the left panels indicate the zero points of the three components with respect to the LSR according to Schönrich et al. (2010).

Table 3
Solar Motion with Respect to the LSR

	(km s^{-1})
$U_\odot$	9.58 ± 2.39
$V_\odot$	10.52 ± 1.96 ($h_R = 2.6$ kpc, $L = 5.2$ kpc)
	10.05 ± 1.98 ($h_R = 2.5$ kpc, $L = 5.0$ kpc)
	13.09 ± 1.85 ($h_R = 3.0$ kpc, $L = 6.0$ kpc)
$W_\odot$	7.01 ± 1.67

Table 4
Vertical Gradient of the Velocity Dispersions at Each T_{eff} Bin

T_{eff} (K)	$d\sigma_U/d|z|$ (km s^{-1} kpc^{-1})	$d\sigma_V/d|z|$ (km s^{-1} kpc^{-1})	$d\sigma_W/d|z|$ (km s^{-1} kpc^{-1})
4250	-0.2 ± 1.4	54.5 ± 3.4	20.7 ± 0.7
4750	10.4 ± 1.7	22.9 ± 2.3	18.9 ± 1.0
5250	12.7 ± 2.1	14.3 ± 0.4	13.1 ± 0.5
5750	14.1 ± 2.9	30.7 ± 1.2	24.6 ± 1.1
6250	21.8 ± 0.4	29.4 ± 7.0	22.3 ± 2.2
6750	23.0 ± 3.4	5.8 ± 0.5	28.4 ± 8.3

derived cross-terms. The velocity dispersions show clear trends along either T_{eff} or $|z|$. First, all three velocity dispersions show an abrupt drop at around $T_{eff} \sim 6000$ K. This sudden drop has been seen in all $|z|$ bins. It is in agreement with the turnaround point in $\langle V \rangle$ shown in the middle left panel of Figure 9. The decreased velocity dispersions for stars with $T_{eff} > 6000$ K again imply that the young stars are less affected by scattering and hence are kinematically cooler.

Second, the velocity dispersions show vertical gradients in most of the T_{eff} bins. Particularly, the vertical gradient of σ_U is correlated with T_{eff}, as shown in the second column of Table 4. Although the vertical gradients of σ_V and σ_W are mostly larger that those of σ_U, they do not show clear trends along T_{eff} (also see Table 4).

The ratios of the velocity dispersions shown in Figure 10 indicate the shape of the velocity ellipsoids. Columns 12 and 13 in Table 8 also list the values of the two ratios. Both the ratios drop with $|z|$ in most T_{eff} bins. The only exception is at

$T_{eff} = 6750$ K, in which the ratios seem not correlated with $|z|$ (Figure 10).

With derived cross-terms, we can also estimate the vertex deviation and the tilt angle at each T_{eff} bin and $|z|$ slice. The definition of the vertex deviation is

$$l_v \equiv \frac{1}{2} \arctan\left(\frac{2\sigma_{UV}^2}{\sigma_U^2 - \sigma_V^2}\right), \tag{18}$$

and the definition of the tilt angle is

$$\alpha \equiv \frac{1}{2} \arctan\left(\frac{2\sigma_{UW}^2}{\sigma_U^2 - \sigma_W^2}\right). \tag{19}$$

The right panels of Figure 9 show the derived cross-terms of the velocity ellipsoids. Their values are listed in Table 8. Figure 11 shows the estimated l_v and α as functions of T_{eff} and $|z|$.
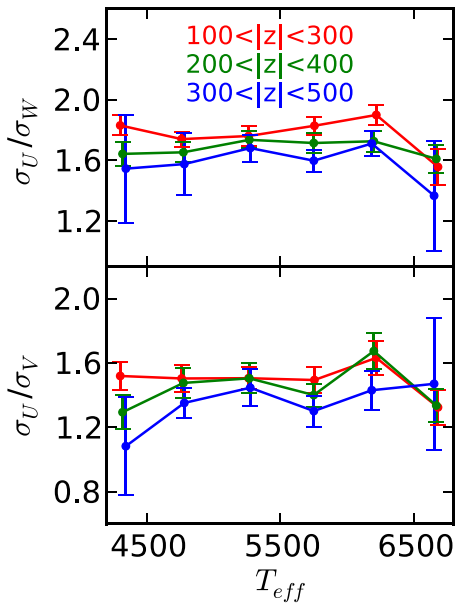
Figure 10. Axis ratios of the ellipsoids in various temperature bins at each $|z|$ slice.
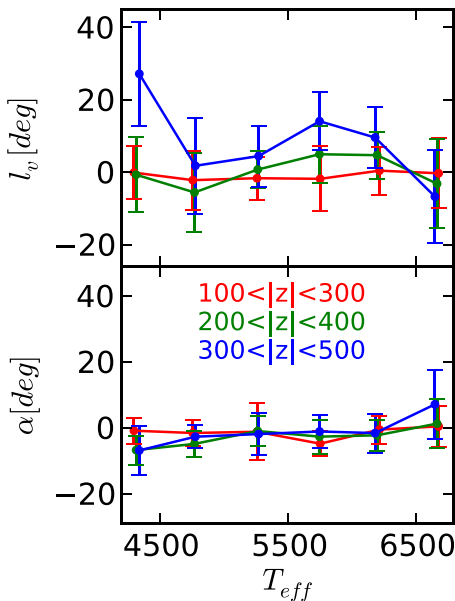

Figure 11. Vertex deviation l_v and tilt angle α in various effective temperature bins at each $|z|$ slice.

We find that l_v varies with $|z|$. It is around 0° for stars with $T_{eff} < 6500$ K at $100 < |z| < 300$ and $200 < |z| < 400$ pc, and then it becomes positive at $300 < |z| < 500$ pc. The vertex deviation for stars with $T_{eff} > 6500$ K as an exception changes with $|z|$ in the opposite sense, i.e., it decreases with $|z|$ from zero to $-6°.7$, although the uncertainty is very large. On the other hand, the tilt angle does not show clear trends with either T_{eff} or $|z|$, which is different from Binney et al. (2014, hereafter B14), who found that the tilt angle changes for the hot dwarfs compared to the giants or cool dwarfs using RAVE (Kordopatis et al. 2013) data. The reason for the discrepancy is hard to investigate, because of the large difference of the volumes between the LAMOST and RAVE data and the difference in methodologies.

4.3. Comparison of the Velocity Ellipsoids with Other Works

Although the volume of our sample at $100 < |z| < 300$ pc does not exactly overlap with that of the sample of DB98, which only extends to 70 pc, we will compare our sample to that of DB98 under the assumption that the velocity dispersions do not largely change from $|z| < 100$ to 300 pc. The color index $B - V$ used by DB98 can be converted into effective temperature according to Sekiguchi & Fukugita (2000). Specifically, the data at around $B - V = 0.412$ (the color index bin 4 in DB98) correspond to $T_{eff} \sim 6600$ K, the data at around $B - V = 0.525$ (bin 6 in DB98) correspond to $T_{eff} \sim 6200$ K, the data at around $B - V = 0.582$ (bin 7 in DB98) correspond to $T_{eff} \sim 5800$ K, and the data at $B - V = 0.719$ (bin 9 in DB98) correspond to $T_{eff} \sim 5200$ K. Because DB98 did not directly show the dispersions along the U, V, and W directions, but showed the dispersions along the major axis of the velocity ellipsoids and the ratio of the major axis to the middle and minor axis, we also rotate the velocity ellipsoid shown in Table 8 and find the longest, middle, and shortest axes of the derived ellipsoids to compare with DB98. Table 5 shows the comparison of the largest velocity dispersion σ_1 and the two ratios of σ_1/σ_2 and σ_1/σ_3 between DB98 and this work. In most cases, the velocity dispersions with roughly the same T_{eff} are slightly larger in our data than those in DB98 by up to ~ 3 km s^{-1}. This is reasonable since the height of the data in this work is slightly larger than those in DB98.

It also shows that the ratio σ_1/σ_2 derived in this work is, on average, consistent with DB98, while σ_1/σ_3 is slightly smaller than DB98. In other words, compared with DB98, the velocity ellipsoid in this work is slightly broader in the z direction, which is probably because the LAMOST data extend over a larger range in $|z|$. Notice that the errors in axis ratios are larger in this work. These errors may be overestimated because they are propagated from the large errors in the cross-terms via the rotation transforms, rather than deriving directly from the observed data.

Surprisingly, for the stars located at $100 < |z| < 300$ pc, the vertex deviation is around zero for all T_{eff} bins. This is inconsistent with the results in DB98. First, it is noted that Sections 3.3.1 and 3.3.2 have shown that the cross-terms of the velocity ellipsoids are the easiest affected in the velocity deprojection method, as McMillan & Binney (2009) have stated. Both the methods in DB98 and in this work are based on the velocity deprojection. Therefore, both the results of the vertex deviation are possibly affected by systematic bias. Because DB98 deprojected the velocity components from the tangental velocities measured from proper motions, while we derive them from the line-of-sight velocities, the systematic bias in both works may go toward different directions. Second, even though we have calibrated the velocity ellipsoid, the corrected σ_{UW} may still slightly bias from their true values (see the top right panels of Figure 8). As a consequence, it is quite hard to compare the vertex deviation between this work and DB98. This issue cannot be easily solved until the three-dimensional velocities of stars are provided.

B14 analyzed the kinematics of $\sim$400,000 RAVE stars and decomposed the sample into hot and cold dwarfs, red clump giants, and non-clump giants. For each of these classes, B14 provided an analytic model for the velocity ellipsoid at each point in the (R, z) plane. With the help of this model, we compared the velocity dispersions between B14 and this work. Table 6 shows the comparison of the largest velocity dispersion

Table 5
Comparison of the Velocity Dispersions between DB98 and This Work

$T_{\rm eff}$	$B - V$	DB98				This Work ($100 < |z| < 300$)			
		σ_1	σ_1/σ_2	σ_1/σ_3	l_v	σ_1	σ_1/σ_2	σ_1/σ_3	l_v
(K)	(mag)	(km s^{-1})			(degree)	(km s^{-1})			(degree)
5250	0.719	$37.20^{+1.41}_{-0.93}$	$1.44^{+0.12}_{-0.12}$	$2.04^{+0.61}_{-0.16}$	$13.1^{+6.7}_{-7.6}$	40.81 ± 5.06	1.51 ± 0.29	1.76 ± 2.05	-1.63 ± 5.90
5750	0.582	$37.64^{+1.37}_{-0.94}$	$1.61^{+0.07}_{-0.18}$	$1.78^{+0.48}_{-0.04}$	$10.2^{+5.6}_{-6.0}$	39.97 ± 5.11	1.50 ± 0.33	1.86 ± 1.21	-1.80 ± 8.98
6250	0.525	$32.93^{+1.09}_{-0.75}$	$1.51^{+0.13}_{-0.12}$	$2.19^{+0.64}_{-0.19}$	$1.9^{+6.0}_{-6.1}$	32.97 ± 5.77	1.62 ± 0.40	1.91 ± 3.11	0.45 ± 6.62
6750	0.412	$26.26^{+0.80}_{-0.59}$	$1.66^{+0.12}_{-0.15}$	$2.16^{+0.52}_{-0.15}$	$10.2^{+5.0}_{-5.4}$	26.05 ± 5.47	1.32 ± 0.44	1.56 ± 2.92	-0.27 ± 9.63

Table 6
Comparison of the Velocity Dispersions between B14 and This Work

Height	$T_{\rm eff}$	B14			This Work		
		σ_1	σ_1/σ_2	σ_1/σ_3	σ_1	σ_1/σ_2	σ_1/σ_3
(pc)	(K)	(km s^{-1})			(km s^{-1})		
$100 < |z| < 300$	>6000	30.47 ± 0.70	1.52 ± 0.11	1.95 ± 0.08	29.51 ± 4.89	1.47 ± 0.21	1.73 ± 0.25
	<6000	38.42 ± 2.30	1.52 ± 0.05	1.71 ± 0.05	40.71 ± 0.54	1.51 ± 0.01	1.80 ± 0.05
$200 < |z| < 400$	>6000	32.70 ± 1.54	1.46 ± 0.19	1.80 ± 0.08	31.20 ± 5.53	1.51 ± 0.25	1.67 ± 0.09
	<6000	43.49 ± 2.77	1.57 ± 0.04	1.75 ± 0.01	42.14 ± 0.80	1.43 ± 0.09	1.70 ± 0.03
$300 < |z| < 500$	>6000	36.57 ± 0.70	1.40 ± 0.18	1.69 ± 0.03	34.23 ± 4.78	1.42 ± 0.06	1.61 ± 0.16
	<6000	48.76 ± 2.50	1.63 ± 0.04	1.67 ± 0.07	42.83 ± 0.76	1.32 ± 0.15	1.62 ± 0.05

σ_1 and the two ratios of σ_1/σ_2 and σ_1/σ_3 between B14 and this work in the different layers. The σ_1, σ_1/σ_2, and σ_1/σ_3 between the two works are in good agreement with each other within 1σ for most cases. However, for stars with $T_{\rm eff} > 6000$ K and $200 < |z| < 400$ and those with $T_{\rm eff} < 6000$ and $300 < |z| < 500$, the two works have differences by about 2σ.

It is not easy to compare the dispersions with S12 since they separate the data into metallicity bins rather than temperature or color index. Moreover, most of the data in S12 are at heights larger than 500 pc, which does not overlap with our data. However, a qualitative comparison is still worthwhile since S12 directly used three velocity components to derive the velocity ellipsoids. First, we compare the velocity dispersions at $300 < |z| < 500$ pc and $T_{\rm eff} = 6250$ K (see Table 8) with the data at $-0.5 <$ [Fe/H] < 0.2 and $\langle z \rangle = -0.69$ kpc in S12, which have $\sigma_R = 38.8^{+1.2}_{-1.3}$ km s^{-1}, $\sigma_\phi = 27.7^{+0.4}_{-0.4}$ km s^{-1}, and $\sigma_z = 22.4^{+0.7}_{-0.7}$ km s^{-1}, and find that they agree with each other. Then, we compare $l_v = 9°.60 \pm 2°.56$ with their result, which is $8°.3 \pm 3°.4$. These two quantities are again consistent with each other. We also compare the tilt angle $\alpha = -1°.73 \pm 0°.76$ with S12, which obtained $-5°.6 \pm 2°.1$. Although the directions of the tilt angles are same, the values have about 2σ difference. This is probably because the tilt angle increases very rapidly with $|z|$ (Büdenbender et al. 2014), and the data in S12 are located in larger $|z|$ than those in this work.

5. DISCUSSION

5.1. The Effect of the Non-Gaussianity of V

It is well known that the V distribution is not Gaussian but has a long tail to the slow side; hence, the Gaussian approximation in Equation (5) may not be correct. It is worthwhile to investigate the systematic bias in the derived velocity ellipsoids due to the Gaussian approximation.

We adopt the analytical form of the distribution function defined by Equation (15) of Cuddeford & Binney (2012), namely,

$$f\left(R, v_R, v_\phi\right) \sim \exp\left(-\frac{v_R^2}{2\sigma_d^2}e^{y v_\phi/v_c}\right)$$
$$\times \exp\left\{\frac{1}{2\sigma_d^2}\Big[v_\phi^2 - v_c^2 \right.$$
$$\left. + 2v_c^2 \ln\left(\frac{v_c}{v_\phi}\right)\Big]e^{y v_\phi/v_c}\right\}, \quad (20)$$

where R is the galactocentric radius, v_R the radial velocity, v_ϕ the azimuthal velocity, and $y \equiv 8/R_d$. The free parameters are R_d, σ_d, and v_c. We predefine three sets of the free parameters and generate three sets of mock data via Monte Carlo simulations. Then we use a Gaussian approximation to estimate the mean v_ϕ and σ_ϕ. In all three simulations, we set $R = 8$ kpc, $v_c = 220$ km s^{-1}, $R_d = 2.5$ kpc. v_R follows a Gaussian distribution with zero mean and sigma of $\sigma_U = \sigma_d \exp(-R/R_d)$. We also add $V_\odot = 12$ km s^{-1} in the simulations. The only varying parameter is σ_d, which is chosen as 80, 110, and 140 km s^{-1}, respectively, for each simulation. We then compare with the directly estimated mean and standard deviation of v_ϕ without assuming a Gaussian profile. The $V_\odot$ is also calculated according to Equations (16) and (17) given $L = 5$ kpc. The comparison is listed in Table 7. This shows that $\langle V \rangle$ is underestimated by a larger amount as σ_d increases. On the other hand, the velocity dispersion estimates from Gaussian fitting are also systematically underestimated by a few km s^{-1}. As a

Table 7
The Test Results of the Non-Gaussianity of V

σ_d	$\langle V \rangle$	σ_V	$V_\odot$ [a]
	(km s^{-1})		
80	-16.6 ± 2.5	12.7 ± 0.5	14.0 ± 2.4
110	-20.2 ± 2.7	19.9 ± 1.1	15.2 ± 2.6
140	-32.0 ± 14.1	33.3 ± 5.6	22.7 ± 13.1
σ_d	$\langle V \rangle_G$	$\sigma_{V,G}$	$V_{\odot,G}$ [b]
	(km s^{-1})		
80	-15.0 ± 2.3	11.9 ± 0.4	12.5 ± 2.3
110	-16.4 ± 2.2	16.7 ± 0.5	11.6 ± 2.2
140	-22.2 ± 10.9	23.5 ± 4.4	14.2 ± 10.3

Notes.
[a] The mean and standard deviation of V are calculated directly from their definitions. The $V_\odot$ is calculated from the direct calculated standard deviation. No Gaussianity is assumed in these derived values.
[b] The mean and sigma values are calculated from fitting a Gaussian profile. And $V_{\odot,G}$ is calculated based on the Gaussian sigma $\sigma_{V,G}$.

consequence, the derived $V_{\odot,G}$ from the Gaussian fitting is also slightly smaller than the true value.

Therefore, we can infer that the $\langle V \rangle$ and σ_V from Equation (5) may be systematically underestimated. The same is true of the estimated $V_\odot$. However, it is worth noting that the velocity distribution function (20) is different than that of the real Galaxy. In reality, this underestimation may be very small and can be negligible. Indeed, the validation test with GCS data shows that the reconstructed V and σ_V are only smaller than the true value within 1 km s^{-1}, as shown in Table 1. Therefore, the $V_\odot$ estimates may be only slightly smaller than the unknown true value. Going from low to high $|z|$, the disk becomes hotter and σ_d increases. Then, the $\langle V \rangle$ is underestimated at higher $|z|$. However, this systematic underestimation likely occurs in all $T_{\rm eff}$ bins and consequently cannot be the reason for the opposite trend along $|z|$ for the stars with $T_{\rm eff} > 6000$ K.

5.2. The Age–$T_{\rm eff}$ Relation

We reveal that the kinematic features for the stars with $T_{\rm eff} > 6000$ K are significantly different from those for the cooler stars. In this section, we first give a theoretical estimation of the age–$T_{\rm eff}$ relation and then discuss the possible reasons why the kinematic features are so different for the stars with $T_{\rm eff} > 6000$ K based on the age distribution in the next section.

In order to derive the age–$T_{\rm eff}$ relation, we first need to know the star formation history of the Milky Way. We adopt the star formation history shown in Figure 1 of Schönrich & Binney (2009), which contains a star formation peak at an age of about 11 Gyr and a star formation rate decreasing with time (see the top panel of Figure 12). Second, we use synthetic isochrones (Marigo et al. 2008) to select the range of $T_{\rm eff}$ for the main-sequence stars at a given age. We also adopt the initial mass function derived by Chabrier (2003) to assign the weight for the main-sequence stars at different temperatures. Finally, we set up the stellar distribution in the age versus $T_{\rm eff}$ plane, as shown in the bottom panel of Figure 12. The blue thick line shows the mean age at different $T_{\rm eff}$. It shows that for the stars with $6500 < T_{\rm eff} < 7000$ K the mean age is between 2 and 3 Gyr and there are almost no stars with age larger than 4 Gyr.

For the stars with $6000 < T_{\rm eff} < 6500$ K the average age varies between 3 and 6 Gyr. For the stars with $T_{\rm eff} < 6000$ K the average age is around 8 Gyr, with a very broad range covering all ages. However, since the star formation rate has a peak at around 11 Gyr, the stars with age older than 8 Gyr dominate this region. The $T_{\rm eff}$ of the abrupt change in age is perfectly consistent with that of the sudden change in the mean velocity and velocity dispersions shown in the left and middle panels of Figure 9. This implies that the Parenago discontinuity occurs at around 6 Gyr. This value is about 3 Gyr earlier than the result by Quillen & Garnett (2001).

5.3. The Asymmetric Motion of the Young Stars

Similar asymmetric motion is also reported in other works. Carlin et al. (2013) found that both the vertical and radial velocities are not at around zero with the LAMOST data. Although the data analyzed by them are located in a larger volume than the data we use in this work, they are qualitatively consistent with the kinematic features of the young stars in our samples. Williams et al. (2013) also found similar trends in the solar vicinity with the red clump stars observed by RAVE (Siebert et al. 2011). Particularly, they found a faster v_ϕ (see their Figure 10); a negative v_R (see their Figure 12), which is equivalent to a net positive U in the Cartesian coordinates; and slightly positive v_Z (see their Figure 13) at the position close to the Galactic midplane. Although the quantitative comparison is quite difficult since the spectral types of the stars in Williams et al. (2013) are completely different and the spatial sampling is also different, the orientations and the values of the offsets in three-dimensional velocity are quite similar to our results. In general, red clump stars are thought to be quite young, and Girardi & Salaris (2001) argued that the peak of the age of nearby red clump stars is only around 1 Gyr. Then, it is not surprising that similar asymmetric motion is found in the red clump samples and the younger stars from our data set.

There are possibly three channels to explain the unusual asymmetric motions for the young stars. We discuss these three scenarios here separately.

First, if the young stars are still not completely relaxed, they may keep the peculiar motion of the molecular cloud in which they are born. Assume that the young stars are formed in a giant molecular cloud containing a total of 10^3–10^4 newly formed stars within a scale of $\sim$200 pc; then the relaxation time for the group of stars is between 0.5 and 4 Gyr. As shown in Figure 12, for the youngest stars with $T_{\rm eff} > 6500$ K even the maximum age is only $\sim$2 Gyr. Therefore, it is possible that these young stars are still not completely relaxed and still display some kinematic features of their birthplace.

Second, it is likely that the young stars are perturbed by the nonaxisymmetric structure in the disk, e.g., the central rotating bar, spiral arms, etc. Some studies have argued that the perturbation must affect both young and old stars (e.g., Famaey et al. 2005). However, in general, orbits of stars in nearly circular orbits and very close to the Galactic midplane can be approximated by three harmonic oscillations in azimuthal, radial, and vertical orientations. Subsequently, the relatively fixed frequencies of the oscillations make the stars more easily respond to the resonance induced by the rotating bar or spiral arms. Since young stars are mostly in near-circular orbits and concentrated in the midplane, they

Table 8
Derived Velocities and the Velocity Ellipsoids from the LAMOST Data

| T_{eff} (K)	$\langle N \rangle$	$\langle U \rangle$	$\langle V \rangle$	$\langle W \rangle$	σ_U	σ_V (km s^{-1})	σ_W	σ_{UV}	σ_{UW}	σ_{VW}	σ_U/σ_V	σ_U/σ_W	l_v (degree)	α (degree)
						$100 < |z| < 300$								
4250	13229	−10.41 ± 1.90	−26.09 ± 1.48	−7.26 ± 0.96	41.25 ± 1.84	27.16 ± 2.11	22.54 ± 1.10	−6.51 ± 10.23	−4.21 ± 7.61	−5.00 ± 15.45	1.52 ± 0.09	1.83 ± 0.07	−0.08 ± 7.41	−0.85 ± 3.92
4750	19593	−8.74 ± 1.49	−25.96 ± 1.52	−7.17 ± 0.92	40.77 ± 1.30	27.12 ± 2.14	23.43 ± 0.91	−5.96 ± 9.15	−5.40 ± 8.12	3.57 ± 7.98	1.50 ± 0.09	1.74 ± 0.05	−2.17 ± 8.12	−1.50 ± 4.05
5250	25805	−8.76 ± 1.41	−26.53 ± 1.68	−6.35 ± 1.23	40.79 ± 1.60	27.10 ± 1.55	23.17 ± 1.26	−5.16 ± 6.28	−4.83 ± 6.01	3.47 ± 8.18	1.51 ± 0.07	1.76 ± 0.07	−1.63 ± 5.90	−1.19 ± 8.58
5750	33453	−8.86 ± 1.40	−26.45 ± 1.62	−5.35 ± 1.19	39.86 ± 1.36	26.68 ± 2.00	21.80 ± 1.04	−5.29 ± 9.62	−9.70 ± 7.09	5.63 ± 5.14	1.49 ± 0.08	1.83 ± 0.06	−1.80 ± 8.98	−4.80 ± 3.86
6250	23565	−8.92 ± 1.50	−21.44 ± 0.93	−3.64 ± 1.16	32.97 ± 1.17	20.21 ± 1.99	17.36 ± 0.95	2.31 ± 6.00	−2.70 ± 12.51	−4.41 ± 6.65	1.63 ± 0.10	1.90 ± 0.07	0.45 ± 6.62	−0.53 ± 4.25
6750	6739	−9.07 ± 1.37	−23.17 ± 1.85	−4.57 ± 1.75	26.05 ± 1.05	19.68 ± 1.97	16.74 ± 1.86	−1.18 ± 9.26	1.79 ± 3.47	1.05 ± 7.94	1.32 ± 0.11	1.56 ± 0.12	−0.27 ± 9.63	0.46 ± 6.22
						$200 < |z| < 400$								
4250	7600	−12.22 ± 2.19	−28.47 ± 2.00	−7.88 ± 1.30	40.79 ± 2.19	31.53 ± 2.86	24.83 ± 1.44	−2.11 ± 12.69	−11.21 ± 9.35	−2.24 ± 8.92	1.29 ± 0.11	1.64 ± 0.08	−0.68 ± 10.41	−6.75 ± 4.42
4750	16639	−8.98 ± 1.47	−29.05 ± 1.91	−6.90 ± 1.00	42.34 ± 2.07	28.69 ± 2.23	25.62 ± 1.09	−9.78 ± 11.28	−9.71 ± 3.75	2.56 ± 11.48	1.48 ± 0.09	1.65 ± 0.06	−5.56 ± 10.81	−4.71 ± 3.95
5250	27523	−8.20 ± 1.87	−28.68 ± 2.05	−6.77 ± 1.98	42.73 ± 1.50	28.40 ± 2.43	24.62 ± 1.05	3.65 ± 4.46	−4.40 ± 5.92	1.80 ± 7.40	1.50 ± 0.09	1.74 ± 0.06	0.76 ± 5.18	−0.91 ± 4.56
5750	36303	−8.08 ± 1.63	−27.97 ± 1.57	−5.73 ± 1.09	42.19 ± 1.47	30.13 ± 1.89	24.61 ± 1.33	8.79 ± 9.63	−7.39 ± 4.78	−2.15 ± 7.90	1.40 ± 0.07	1.71 ± 0.06	4.99 ± 7.87	−2.66 ± 5.12
6250	18621	−7.39 ± 1.41	−19.89 ± 1.29	−4.01 ± 0.95	35.02 ± 1.50	20.92 ± 2.14	20.29 ± 1.09	8.12 ± 3.20	−5.66 ± 6.71	−0.44 ± 5.57	1.67 ± 0.11	1.73 ± 0.07	4.73 ± 6.51	−2.25 ± 4.76
6750	3436	−6.49 ± 1.54	−20.47 ± 1.77	−5.28 ± 1.40	27.27 ± 1.39	20.42 ± 1.77	16.94 ± 1.34	−4.24 ± 10.13	3.21 ± 4.88	−1.41 ± 7.43	1.34 ± 0.10	1.61 ± 0.09	−3.16 ± 12.35	1.29 ± 7.38
						$300 < |z| < 500$								
4250	3797	−10.58 ± 3.25	−35.84 ± 6.44	−7.49 ± 2.78	41.21 ± 10.82	38.06 ± 5.93	26.67 ± 6.46	9.62 ± 17.82	−11.10 ± 10.02	0.34 ± 9.78	1.08 ± 0.31	1.55 ± 0.36	27.20 ± 14.35	−7.01 ± 7.32
4750	11443	−9.37 ± 2.04	−32.45 ± 2.79	−6.33 ± 1.06	42.85 ± 2.12	31.70 ± 2.44	27.20 ± 5.43	5.96 ± 9.46	−7.46 ± 4.18	0.07 ± 9.94	1.35 ± 0.09	1.58 ± 0.21	1.80 ± 13.30	−2.90 ± 3.53
5250	22503	−9.03 ± 2.08	−30.24 ± 2.10	−6.98 ± 2.03	43.33 ± 2.80	29.96 ± 2.79	25.78 ± 1.56	8.68 ± 8.89	−6.24 ± 11.04	−4.10 ± 9.81	1.45 ± 0.11	1.68 ± 0.09	4.47 ± 8.44	−1.84 ± 6.28
5750	33595	−8.92 ± 1.62	−29.11 ± 1.35	−5.85 ± 1.39	42.68 ± 2.17	32.81 ± 2.67	26.71 ± 1.39	14.13 ± 7.54	−4.91 ± 2.45	−2.65 ± 8.72	1.30 ± 0.10	1.60 ± 0.07	14.10 ± 8.03	−1.25 ± 4.87
6250	13986	−8.40 ± 1.78	−18.99 ± 1.88	−4.64 ± 1.05	37.32 ± 2.01	26.09 ± 2.84	21.81 ± 1.32	11.13 ± 5.17	−5.26 ± 3.04	−3.20 ± 7.56	1.43 ± 0.12	1.71 ± 0.08	9.60 ± 8.41	−1.73 ± 5.93
6750	1566	−7.24 ± 2.09	−17.39 ± 1.81	−6.62 ± 1.91	30.64 ± 7.05	20.84 ± 7.12	22.42 ± 6.33	−7.45 ± 9.12	7.57 ± 11.32	2.71 ± 5.20	1.47 ± 0.41	1.37 ± 0.36	−6.71 ± 12.79	7.36 ± 10.43
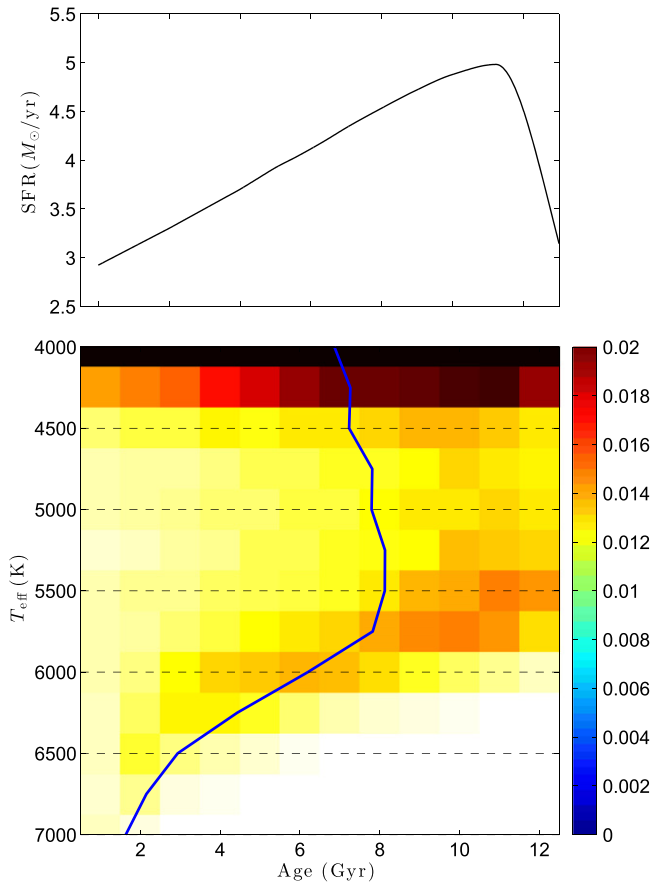
Figure 12. Top: star formation history used by Schönrich & Binney (2009). Bottom: stellar distribution in the $T_{\rm eff}$ vs. age plane for the main-sequence stars based on the Chabrier initial mass function (Chabrier 2003) and the synthetic stellar isochrones (Marigo et al. 2008). The color codes the normalized stellar distribution, and the blue thick line indicates the mean age as a function of $T_{\rm eff}$. The dashed lines indicate the separation of the $T_{\rm eff}$ bins in this work.

are more easily perturbed by nonaxisymmetric structures than the old stars. However, the bar and spiral structures are mostly in the Galactic midplane and thus may not affect the vertical motion of the young stars (though for some mechanisms by which the bar and spiral arms can vertically perturb the disk see Debattista 2014; Faure et al. 2014). Therefore, it is hard to explain why the young stars also show a net positive value in W.

Finally, the disk may have been perturbed by a merging event. Indeed, Widrow et al. (2012) and Yanny & Gardner (2013) found that the stellar vertical density shows wave-like features, which could be the density wave excited by a minor merger (Gómez et al. 2013).

Certainly, none of the scenarios discussed above can be easily ruled out. Further observational and theoretical works are required to better address this challenging issue.

An interesting question raised here is why previous studies of local kinematics based on the *Hipparcos* data do not show the asymmetric motion. This is quite hard to answer. The different volume of the *Hipparcos* may be one reason. More detailed investigations with the future *Gaia* data including accurate distance estimates and 3D velocities (Perryman et al. 2001) may be needed to complete the picture of local disk kinematics.

5.4. The Impact of Systematic Bias in the Distance and Radial Velocity

Although Figure 1 does not show any dependence of the distance estimates on $T_{\rm eff}$, some extreme tests, e.g., the distance is only over- or underestimated for the warmer stars but unchanged for the cooler ones, are very helpful to verify whether the kinematic results are robust. The left and middle panels of Figure 13 show the mean velocities derived from the distances with artificial 20% over- and underestimation only for the stars with $T_{\rm eff} > 6000$ K, respectively. Essentially, the asymmetric motions of the young stars still exist in both $\langle U \rangle$ and $\langle W \rangle$ with slightly shifted values. And Parenago's discontinuity and the turnover phenomenon in $\langle V \rangle$ are still substantial. We also do not find any systematic bias due to the over- or underestimation of the distance in the velocity ellipsoids.

Figure 6 presents a weak anticorrelation between the offset of the radial velocities and $T_{\rm eff}$. This drives us to further investigate whether the results are stable when the offset varies with $T_{\rm eff}$. We then fit the offset of the radial velocity with a linear function of $T_{\rm eff}$ and correct the radial velocities for the individual stars with the $T_{\rm eff}$-independent offset. We find that this leads to slight shifts in $\langle U \rangle$, $\langle V \rangle$, and $\langle W \rangle$, as shown in the right panels of Figure 13. Although the difference in $\langle U \rangle$ between the young and old stars has vanished, the differences in $\langle V \rangle$ and $\langle W \rangle$ are even stronger. It may also shift the derived local motion of the Sun. For $U_\odot$, it may decrease by ~ 1 km s^{-1}, and for $W_\odot$, it may increase by ~ 1 km s^{-1}. These shifts are within 1σ uncertainties according to Table 3. We also notice that Gao et al. (2015) found that the offset is 3.8 km s^{-1} compared to the LAMOST data with the PASTEL catalog (Soubiran et al. 2010), implying that the calibration of the radial velocity may also depend on different calibrators. We performed another test with the offset of 3.8 km s^{-1} and found that the mean velocities shift by ~ 1 km s^{-1} for all stars and the systematic differences between the young and old stars are unchanged. Therefore, in order to maintain simplification, we adopt the correction of the radial velocity with a constant 5.7 km s^{-1} for all stars in this work. According to the tests with various corrections, we conclude that the differences in $\langle V \rangle$ and $\langle W \rangle$ between the young and old stars are real, while the mild difference in $\langle U \rangle$ shown in Figure 9 may be insignificant.

6. CONCLUSIONS

We use the nearby FGK-type main-sequence stars selected from LAMOST DR1 data to estimate the three-dimensional velocities and velocity ellipsoids from line-of-sight velocities alone. It has been known that the velocity deprojection technique can introduce systematic bias due to the spatial variation of the velocity dispersions. Moreover, we find that the uneven spatial sampling can affect the velocity dispersion as well. In order to derive the corrected velocity ellipsoid from the deprojection method, we calibrate it using a set of transform matrices estimated from simulations. The calibration works well in the simulations and then is applied to the observed data.

We associate the derived velocities and their ellipsoids with the effective temperature and $|z|$ and reveal that the asymmetric motions of the stars in the solar neighborhood reported by previous works are mainly seen among warm stars with $T_{\rm eff} > 6000$ K, which are very young, with an average age of less than 4 Gyr. These young stars rotate faster in larger $|z|$ than in smaller $|z|$. Meanwhile, they move up toward the north Galactic
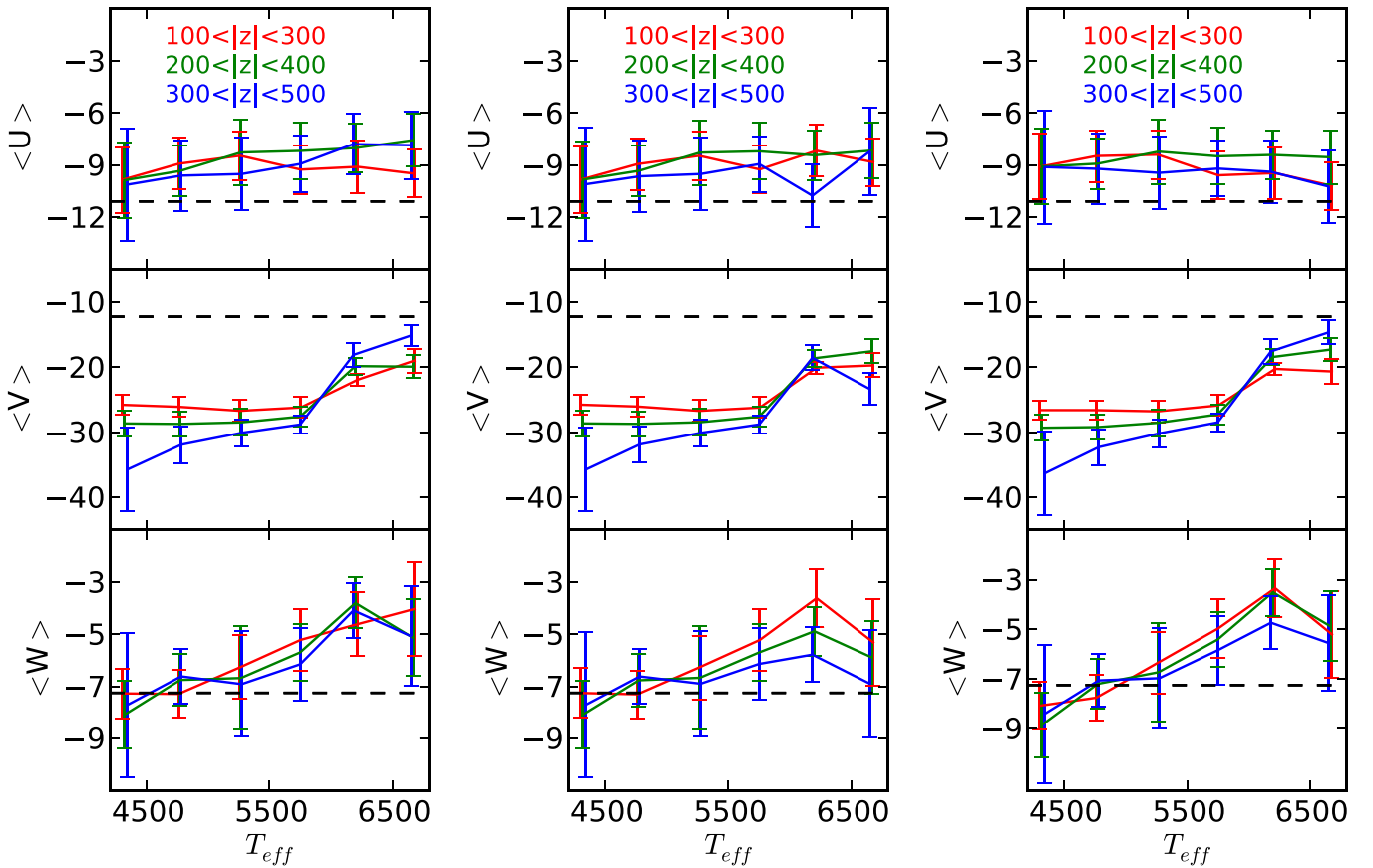
Figure 13. Mean velocities with different systematically biased distance and radial velocity. The left panels are the results with overestimated distance by a factor of 20%; the middle panels are the results with underestimated distance by a factor of 20% only in the bins with $T_{\rm eff} > 6000$ K and keep the distances in other bins unchanged; and the right panels are the results with the offset varying as an anticorrelation function of $T_{\rm eff}$ presented in Figure 6 in the radial velocity distribution.

pole by about 3 km s^{-1} and probably radially inward to the Galactic center by a few km s^{-1}. The nature of the asymmetric motion is still not clear. With the older (cool) stars, we give estimates of the solar motion with respect to the LSR. We obtain $(U_\odot, V_\odot, W_\odot) = (9.58 \pm 2.39, 10.75 \pm 1.96, 7.01 \pm 1.67)$ km s^{-1}.

We also derive the velocity ellipsoids and find that the young stars have significantly smaller dispersions than the older stars. The vertical gradient of the velocity dispersions is larger in σ_V and σ_W than in σ_U. On the other hand, σ_U shows clear correlation with $T_{\rm eff}$, but the other two dispersions do not. We confirm that the Parenago discontinuity occurs at about 6 Gyr by comparing the velocity dispersions with a simple star formation model.

The derived velocity ellipsoids in this work are essentially consistent with those in DB98, S12, and B14. The velocity deprojection method may still slightly suffer from the distortion in the derived cross-terms even after calibration. Therefore, more accurate estimations about the orientation of the velocity ellipsoid should be done with three-dimensional velocities.

REFERENCES

Ahn, C. P., Alexandroff, R., Allende Prieto, C., et al. 2014, ApJS, 211, 17
Antoja, T., Helmi, A., Bienayme, O., et al. 2012, MNRAS, 426, 1
Antoja, T., Figueras, F., Romero-Gómez., M., et al. 2011, MNRAS, 418, 1423
Binney, J., & Tremaine, S. 2008, Galactic Dynamics (2nd ed.; Princeton, NJ: Princeton Univ. Press)
Binney, J. J., Burnett, B., Kordopatis, G., et al. 2014, MNRAS, 439, 1231B
Bovy, J., Nidever, D. L., Rix, H.-W., et al. 2014, ApJ, 790, 127
Büdenbender, A., van de Ven, G., & Watkins, L. L. 2014, arXiv:1407.4808
Carlin, J. L., DeLaunay, J., Newberg, H. J., et al. 2013, ApJ, 777, 5
Carlin, J. L., Liu, C., Newberg, H. J., et al. 2015, AJ, 150, 4
Chabrier, G. 2003, PASP, 115, 763
Cuddeford, P., & Binney, J. 2012, MNRAS, 266, 273
Cui, X. Q., Zhao, Y. H., Chu, Y. Q., et al. 2012, RAA, 12, 1197
Debattista, V. P. 2014, MNRAS, 443, L1
Dehnen, W. 1998, AJ, 115, 2384

Dehnen, W. 2000, AJ, 119, 800
Dehnen, W., & Binney, J. J. 1998, MNRAS, 298, 387
Deng, L. C., Newberg, H. J., Liu, C., et al. 2012, RAA, 12, 735
Famaey, B., Jorissen, A., Luri, X., et al. 2005, A&A, 430, 165
Faure, C., Siebert, A., & Famaey, B. 2014, MNRAS, 440, 2564
Foreman-Mackey, D., Hogg, D. W., Lang, D., & Goodman, J. 2012, ApJ, 752, 147
Fuchs, B., Dettbarn, C., Rix, H. W., et al. 2009, AJ, 137, 4149
Fux, R. 2001, A&A, 373, 511
Gao, H., Zhang, H., Xiang, M., et al. 2015, RAA, submitted
Gao, S., Liu, C., Zhang, X. B., et al. 2014, ApJ, 788, 37
Gilmore, G., Randich, S., Asplund, M., et al. 2012, Msngr, 147, 25
Girardi, L., & Salaris, M. 2001, MNRAS, 323, 109
Gómez, F. A., Minchev, I., O'Shea, B. W., et al. 2013, MNRAS, 429, 159
Goodman, J., & Weare, J. 2010, Comm. App. Math. Comp. Sci., 5, 65
Holmberg, J., Nordström, B., & Anderson, J. 2007, A&A, 501, 941
Huang, Y., Liu, X.-W., Yuan, H.-B., et al. 2015, MNRAS, 449, 162
Jenkins, A. 1992, MNRAS, 257, 620
Jurić, M., Ivezić, Ž., Brooks, A., et al. 2008, ApJ, 673, 864
Kordopatis, G., Gilmore, G., Steinmetz, M., et al. 2013, AJ, 146, 134
Marigo, P., Girardi, L., Bressan, A., et al. 2008, A&A, 482, 883
McMillan, P. J., & Binney, J. J. 2009, MNRAS, 400, 103
Nordström, B., Mayor, M., Andersen, J., et al. 2004, A&A, 418, 989
Parenago, P. P. 1950, AZh, 27, 150
Perryman, M. A. C., de Boer, K. S., Gilmore, G., et al. 2001, A&A, 369, 339

Quillen, A. C., & Garnett, D. R. 2001, in ASP Conf. Ser. 230, Galaxy Disks and Disk Galaxies, ed. G. Jose, S. J. Funes & E. M. Corsini (San Francisco, CA: ASP), 87
Recio-Blanco, A., de Laverny, P., Kordopatis, G., et al. 2014, A&A, 567, A5
Roman, N. G. 1950, ApJ, 112, 554
Roman, N. G. 1952, ApJ, 116, 122
Röser, S., Demleitner, M., & Schilbach, E. 2010, AJ, 139, 244
Schönrich, R., & Binney, J. 2009, MNRAS, 396, 203
Schönrich, R., & Binney, J. 2012, MNRAS, 419, 1546
Schönrich, R., Binney, J., & Dehnen, W. 2010, MNRAS, 403, 1829
Schwarzschild, K. 1908, Göttingen Nachr., 191
Sekiguchi, M., & Fukugita, M. 2000, AJ, 120, 1072
Sharma, S., Bland-Hawthorn, J., Binney, J., et al. 2014, ApJ, 793, 51
Siebert, A., Bienaym'e, O., Binney, J., et al. 2008, MNRAS, 391, 793
Siebert, A., Williams, M. E. K., Siviero, A., et al. 2011, AJ, 141, 187
Smith, M. C., Whiteoak, S. H., & Evans, N. W. 2012, ApJ, 746, 181
Soubiran, C., Le Campion, J.-F., Cayrel de Strobel, G., & Caillo, A. 2010, A&A, 515, 111
van der Kruit, P. C., & Freeman, K. C. 2011, ARA&A, 49, 301
Widrow, L. M., Gardner, S., Yanny, B., et al. 2012, ApJ, 750, 41
Williams, M. E. K., Steinmetz, M., Binney, J., et al. 2013, MNRAS, 436, 101
Xia, Q. R., Liu, C., Mao, S., et al. 2014, MNRAS, 447, 2367
Yanny, B., & Gardner, S. 2013, ApJ, 777, 91
Zacharias, N., Finch, C. T., Girard, T. M., et al. 2013, AJ, 145, 44
Zhao, G., Zhao, Y. H., Chu, Y. Q., et al. 2012, RAA, 12, 723
Zhao, J. K., Zhao, G., & Chen, Y. Q. 2009, ApJ, 692, 113